Mon. Not. R. Astron. Soc. **396,** 203–222 (2009) doi:10.1111/j.1365-2966.2009.14750.x

Chemical evolution with radial mixing

Ralph Schönrich[1]★ and James Binney[2]

[1]*Universitätssternwarte München, Scheinerstr. 1, D-81679 München, Germany*
[2]*Rudolf Peierls Centre for Theoretical Physics, Keble Road, Oxford OX1 3NP*

Accepted 2009 March 5. Received 2009 March 5; in original form 2008 September 4

ABSTRACT

Models of the chemical evolution of our Galaxy are extended to include radial migration of stars and flow of gas through the disc. The models track the production of both iron and α-elements. A model is chosen that provides an excellent fit to the metallicity distribution of stars in the Geneva–Copenhagen survey (GCS) of the solar neighbourhood and a good fit to the local Hess diagram. The model provides a good fit to the distribution of GCS stars in the age–metallicity plane, although this plane was not used in the fitting process. Although this model's star formation rate is monotonically declining, its disc naturally splits into an α-enhanced thick disc and a normal thin disc. In particular, the model's distribution of stars in the ([O/Fe], [Fe/H]) plane resembles that of Galactic stars in displaying a ridge line for each disc. The thin-disc's ridge line is entirely due to stellar migration, and there is the characteristic variation of stellar angular momentum along it that has been noted by Haywood in survey data. Radial mixing of stellar populations with high σ_z from inner regions of the disc to the solar neighbourhood provides a natural explanation of why measurements yield a steeper increase of σ_z with age than predicted by theory. The metallicity gradient in the interstellar medium is predicted to be steeper than in earlier models, but appears to be in good agreement with data for both our Galaxy and external galaxies. The models are inconsistent with a cut-off in the star formation rate at low gas surface densities. The absolute magnitude of the disc is given as a function of time in several photometric bands, and radial colour profiles are plotted for representative times.

Key words: galaxies: abundances – galaxies: evolution – galaxies: ISM – galaxies: kinematics and dynamics – Galaxy: disc – solar neighbourhood.

1 INTRODUCTION

Models of the chemical evolution of galaxies are key tools in the push to understand how galaxies formed and have evolved. Their application to our Galaxy is of particular importance both on account of the wealth of observational data that they can be required to reproduce and on account of the inherent interest in deciphering the history of our environment.

From the pioneering papers by van den Bergh (1962) and Schmidt (1963), it has generally been assumed that a galaxy such as the Milky Way can be divided into concentric cylindrical annuli, each of which evolves independently of the others (e.g. Pagel 1997; Chiappini, Matteucci & Gratton 1997; Chiappini, Matteucci & Romano 2001; Naab & Ostriker 2006; Colavitti, Matteucci & Murante 2008). The contents of any given cylinder are initially gaseous and of extremely low or zero metallicity. Over time, stars form in the cylinder and the more massive ones die, returning a mixture of heavy elements to the remaining gas. The consequent increase in the metallicity of the gas and newly formed stars is generally moderated by an inflow of gas from intergalactic space, and, less often, by an outflow of supernova-heated gas.

The cool, star-forming gas within any cylinder is assumed to be well mixed, so at any time it can be characterized by a metallicity $Z(r, t)$, where r is the cylinder's radius. Hence, the stars formed within a given cylinder should have metallicities $Z(r, t_\mathrm{f})$ that are uniquely related to their time of formation, t_f. Observations do not substantiate this prediction; in fact, Edvardsson et al. (1993) showed that solar-neighbourhood stars are widely distributed in the (t_f, Z) plane [for a detailed discussion see Haywood (2006) and Section 6.2].

The absence of an age–metallicity relation in the solar neighbourhood is naturally explained by radial migration of stars (Sellwood & Binney 2002; Haywood 2008; Roskar et al. 2008b). It has been recognized for many years that scattering by spiral structure and molecular clouds gradually heats the stellar disc, moving stars on to ever more eccentric and inclined orbits. Stars that are on eccentric orbits clearly contribute to different cylindrical annuli at different

★E-mail: rasch@usm.lmu.de

phases of their orbits, and thus tend to modify any radial gradient in the metallicities of newly formed stars. Moreover, scattering events also change the guiding centres of stellar orbits, so even a star on a circular orbit can be found at a different radius from that of its birth. In fact, Sellwood & Binney (2002) argued that the dominant effect of transient spiral structure is resonant scattering of stars across the structure's corotation resonance, so even a star that is still on a near-circular orbit may be far from its radius of birth. Roskar et al. (2008a) showed that in a cosmological simulation of galaxy formation that included both stars and gas, resonant scattering at corotation caused stars to move outwards and gas inwards, with the result that the stellar disc extended beyond the outer limit of star formation; the outer disc was entirely populated by stars that had formed much further in and yet were still on nearly circular orbits. This simulation confirmed the conjecture of Sellwood & Binney (2002) that gas would participate in resonant scattering alongside stars.

We distinguish two drivers of radial migration: when the angular momentum of a star is changed, whether by scattering at an orbital resonance or by non-resonant scattering by a molecular cloud, the star's guiding-centre radius changes and the star's entire orbit moves inwards or outwards depending on whether angular momentum is lost or gained. When a scattering event increases a star's epicycle amplitude without changing its angular momentum, the star contributes to the density over a wider range of radii. In a slight modification of the terminology introduced by Sellwood & Binney (2002), we say that changes in angular momentum cause 'churning' while changes in epicycle amplitude lead to 'blurring'. This paper extends models of Galactic chemical evolution to include the effects of churning and blurring.

Given the strength of the arguments that cold gas should participate in churning alongside stars, and that shocks induced by spiral structure cause gas to drift inwards, it is mandatory simultaneously to extend traditional chemical evolution models to include radial flows of gas within the disc. Lacey & Fall (1985) studied chemical evolution in the presence of a radial inflow of gas and demonstrated that a radial flow enhances the metallicity gradient within the disc. This enhancement plays an important role in our models, which differ from those of Lacey & Fall in that they include both radial gas flows and radial migration of stars. Moreover, we can fit our models to observational data that are much richer than that available to Lacey & Fall (1985).

Our models are complementary to ab initio models of galaxy formation such as those presented by Samland & Gerhard (2003) and Roskar et al. (2008b) in that they allow the solar neighbourhood to be resolved in greater detail, and because they are enormously less costly numerically, they permit parameter searches to be made that are not feasible with ab initio models.

The paper is organized as follows. Section 2 presents the equations upon which the models are based. These consist of the rules that determine the rate of infall of fresh gas, the rate of star formation, details of the stellar evolution tracks and chemical yields that we have used and descriptions of how churning and blurring are implemented. Section 3 describes in some detail a 'standard' model of the evolution of the Galactic disc. This covers its global properties but focuses on what would be seen in a survey of the solar neighbourhood. Section 4 presents the details of the selection function that is required to mimic the Geneva–Copenhagen survey (GCS) sample of solar-neighbourhood stars published by Nordström et al. (2004) and Holmberg, Nordström & Andersen (2007), and explains how this sample has been used to constrain the model's parameters. Section 5 explains how the observable properties of the model depend on its parameters. Section 6 discusses the relation of the present models to earlier ones, and discusses the extent to which it is consistent with the analysis of solar-neighbourhood data by Haywood (2008). Section 7 sums up.

2 GOVERNING EQUATIONS

The simulation is advanced by a series of discrete time-steps of 30 Myr duration.

The disc is divided into 80 annuli of width 0.25 kpc and central radii that range from 0.125 to 19.875 kpc. In each annulus, there is both 'cold' ($\sim$30 K) and 'warm' ($\gtrsim 10^4$ K) gas with specified abundances (Y, Z) of helium and heavy elements. The 'warm gas' is not available for star formation and should be understood to include both inter-cloud gas within the plane and extraplanar gas, which probably contains a significant fraction of the Galaxy's interstellar medium (ISM). Indeed, in NGC 891, a galaxy similar to the Milky Way, of the order of a third of H I, is extraplanar (Oosterloo et al. 2007). In the Milky Way, this gas would constitute the 'intermediate-velocity clouds' that are observed at high and intermediate Galactic latitudes (Kalberla & Dedes 2008).

Within the heavy elements, we keep track of the abundances of O, C, Mg, Si, Ca and Fe. Each annulus has a stellar population for each elapsed time-step, and this population inherits the abundances Y, Z, etc., of the local cold gas. At each stellar mass, the stellar lifetime is determined by the initial abundances, and at each age we know the luminosity and colours of such of its stars that are not yet dead. Each stellar population is at all times associated with the annulus of its birth; the migration of stars is taken into account as described below only when returning matter to the ISM or constructing an observational sample of stars.

2.1 Metallicity scale

The whole field of chemical modelling has been thrown into turmoil by the discovery that three-dimensional, non-equilibrium models of the solar atmosphere require the metal abundance of the Sun to be $Z_\odot = 0.012$–0.014 (Grevesse, Asplund & Sauval 2007) rather than the traditional value $\sim$0.019. This work suggests that the entire metallicity scale needs to be thoroughly reviewed: if the Sun's metallicity has to be revised downwards, then so will the metallicities of most nearby stars. Crucially, there is the possibility that values for the metallicity of the ISM require revision: some values derive from measurements of the metallicities of short-lived stars such as B stars and require downwards revision (e.g. Daflon & Cunha 2004), while others are inferred from measurements of the strengths of interstellar emission lines, and are not evidently affected by changes in stellar metallicities. If the metallicity scale of stars were lowered while that of the ISM remained substantially unaltered, it would be exceedingly hard to construct a viable model of the chemical evolution of the solar neighbourhood. Moreover, both the stellar catalogue and most of the measurements of interstellar abundances with which we wish to compare our models are on the old metallicity scale, and unphysical anomalies will become rife as soon as one mixes values on the old scale with ones on the new. Therefore, for consistency we use the old solar abundance $Z_\odot = 0.019$ and exclude from considerable metallicity values that are on the new scale.

2.2 Star formation law

Stars form according to the Kennicutt (1998) law. Specifically, with the surface density of cold gas $\Sigma_{\rm g}$ measured in $\mathrm{M}_\odot\,\mathrm{pc}^{-2}$ and t in Myr, star formation increases the stellar surface density at a rate

$$\frac{\mathrm{d}\Sigma_*}{\mathrm{d}t} = 1.2\times10^{-4}\begin{cases}\Sigma_{\rm g}^{1.4} & \text{for}\quad \Sigma_{\rm g} > \Sigma_{\rm crit}\\ C\Sigma_{\rm g}^{4} & \text{otherwise,}\end{cases} \tag{1}$$

where the threshold for star formation, $\Sigma_{\rm crit}$, is a parameter of the model and $C = \Sigma_{\rm crit}^{-2.6}$ ensures that the star formation rate (SFR) is a continuous function of surface density. The normalization in equation (1) was chosen to yield the observed surface densities of gas and stars near the Sun.

The stars are assumed to be distributed in initial mass over the range $(0.1,\ 100)\,\mathrm{M}_\odot$ according to the Salpeter function, $\mathrm{d}N/\mathrm{d}M \propto M^{-2.35}$. The luminosities, effective temperatures, colours and lifetimes of these stars are taken by linear interpolation in (Y, Z) from the values given in the BaSTI (A Bag of Stellar Tracks and Isochrones) data base (Pietrinferni et al. 2004).

2.3 Return of metals

The nucleosynthetic yields of individual metals are in many cases still subject to significant uncertainties (e.g. Thomas, Greggio & Bender 1998); in fact, models of the chemical evolution of the solar neighbourhood have been used to constrain these yields (Francois et al. 2004).

For initial masses in the ranges 5–11 and 35–100 $\mathrm{M}_\odot$, values of X, Y, Z,C and O were taken from Maeder (1992) using a non-linear interpolation scheme: the paper gives yields $Y_{\rm LZ}$ for a low metallicity ($Z = 10^{-4}$) and yields $Y_{\rm HZ}$ for a high metallicity ($Z = 0.02$). Guided by the metallicity-dependence of the sizes of CO cores reported by Portinari, Chiosi & Bressan (1998), we take

$$Y(Z) = (1-\alpha)Y_{\rm LZ} + \alpha Y_{\rm HZ}, \tag{2}$$

where

$$\alpha = \begin{cases} 0 & \text{for}\quad Z < 0.005\\ 320(Z-0.005) & \text{for}\quad 0.005 < Z < 0.0075\\ 0.8 + 16(Z-0.0075) & \text{for}\quad 0.0075 < Z < 0.02\\ 1 & \text{for}\quad Z > 0.02.\end{cases} \tag{3}$$

The yields of elements other than X, Y, Z,C and O from stars with masses in this range were taken from the *ORFEO* data base of Limongi & Chieffi (2008) with the mass cut set such that 0.05 $\mathrm{M}_\odot$ of ^{56}Ni is produced; this relatively low mass cut reproduces the Ca/Fe ratio measured in very metal-poor stars by Lai et al. (2008). Stars less massive than 10 $\mathrm{M}_\odot$ were assumed to produce no elements heavier than O. For stars with masses $<5\,\mathrm{M}_\odot$, the yields were taken by linear interpolation from Marigo (2001).

For initial stellar masses in the range 11–35 $\mathrm{M}_\odot$, we used the metallicity-dependent yields of heavy elements from Chieffi & Limongi (2004) by linear interpolation on mass and metallicity, extrapolating up to $\alpha = 1.5$ or $Z = 0.03$, respectively. Chieffi & Limongi (2004) used a relatively high mass cut, which produced 0.1 $\mathrm{M}_\odot$ of ^{56}Ni. With our interpolation, the average amount of ^{56}Ni produced is well within the expected range.

A fraction $f_{\rm eject}$ of the gas ejected by dying stars leaves the Galaxy; we tested models with $0 \le f_{\rm eject} \le 0.05$ (Pagel 1997). Increasing $f_{\rm eject}$ has the effect of reducing the final metallicity of the disc; in fact, there is almost complete degeneracy between the values of $f_{\rm eject}$ and nucleosynthetic yields. In view of the evidence that star formation near the Galactic centre drives a Galactic wind (Bland-Hawthorn & Cohen 2003), we set $f_{\rm eject} = 0.15$ at $R < 3.5$ kpc in models that use the accretion law (6) below. At all other radii we set $f_{\rm eject} = 0.04$.

A fraction $f_{\rm direct}$ of the ejecta goes straight to the cold gas reservoir of the local annulus, and the balance goes to the annulus's warm-gas reservoir. Setting $f_{\rm direct}$ to values of $\sim$0.2 has a significant impact on the number of extremely metal-poor stars predicted near the Sun. However, such large values of $f_{\rm direct}$ are not well motivated physically, and in the models presented here $f_{\rm direct} = 0.01$ has a negligible value.

In each time-step δt, a fraction $\delta t/t_{\rm cool}$ of the 'warm' gas (which includes extraplanar gas) transfers to the cold-gas reservoir from which stars form. The parameter $t_{\rm cool}$ is determined by the dynamics of extraplanar gas and the balance between radiative cooling and shock heating within the plane. Consequently, its value cannot be determined a priori from atomic physics. Increasing $t_{\rm cool}$ increases the mass of 'warm' gas and delays the incorporation of freshly made metals into new stars, so the number of very metal-poor stars formed increases with $t_{\rm cool}$. Although of the order of a quarter of the neutral hydrogen of NGC 891 is extraplanar (Oosterloo et al. 2007), some of this gas will be formerly cold interstellar gas that has been shock accelerated by stellar ejecta. We do not model shock heating of cold gas, and replenish the warm-gas reservoir exclusively with stellar ejecta (from stars of every mass). Hence, the warm-gas reservoir should be less massive than the sum of the extraplanar and warm in-plane bodies of gas in a galaxy like NGC 891. We have worked with values $t_{\rm cool} \gtrsim 1$ Gyr that yield warm-gas fractions of the order of 10 per cent. The results of the models are not sensitive to the value of $t_{\rm cool}$.

There is abundant evidence that pristine intergalactic gas disappeared from the intergalactic medium (IGM) long ago: quasar absorption-line studies reveal an early build up of heavy elements in the IGM (Pettini et al. 2003). While it is clear that the disc formed from material that had been enriched by pregalactic and halo stars, it is unclear what abundances this material had. We take the chemical composition of the pre-enriched gas to be that of the 'warm' ISM after two time-steps, starting with $5\times10^8\,\mathrm{M}_\odot$ of pristine gas. In each of the following four time-steps, a further $1.25\times10^8\,\mathrm{M}_\odot$ of gas with this metallicity is added to the disc. The surface density of the added gas is proportional to

$$\left(1.0 - \mathrm{e}^{(R-19.8\,\mathrm{kpc})/11.8\,\mathrm{kpc}}\right)\mathrm{e}^{-R/4\,\mathrm{kpc}}. \tag{4}$$

Thus, the surface density is exponential with scalelength 4 kpc inside $\sim R_0$ but tapered to zero at the outer edge of the grid. The existence at the outset of a warm, pre-enriched component of the ISM is physically well motivated and proves the most effective way of producing the right number of metal-poor stars.

Type Ia supernovae are included by assuming that 7.5 per cent of the mass in white dwarfs formed by stars of initial mass between 3.2 and 8.5 $\mathrm{M}_\odot$ ultimately explodes in Type Ia supernovae. The yields were taken to be those of the W70 model in Iwamoto et al. (1999). It is believed that the progenitors of Type Ia supernovae have lifetimes of the order of a Gyr (Förster et al. 2006), and we have taken the mass $M_{\rm WD}$ of the population that survives to time t from white-dwarf formation to satisfy

$$\frac{\mathrm{d}M_{\rm WD}}{\mathrm{d}t} = \begin{cases}0 & \text{for}\quad 0 < t \le 0.15\,\mathrm{Gyr}\\ -M_{\rm WD}/1.5\,\mathrm{Gyr} & \text{for}\quad T > 0.15\,\mathrm{Gyr.}\end{cases} \tag{5}$$

The rate of Type Ia SNe is constrained by the requirements that (i) [O/Fe] has to fall from $\sim$0.6 for the oldest stars to around -0.1, and (ii) [Ca/Fe] should go from about $\sim$0.3 to $\sim$0. The full curve

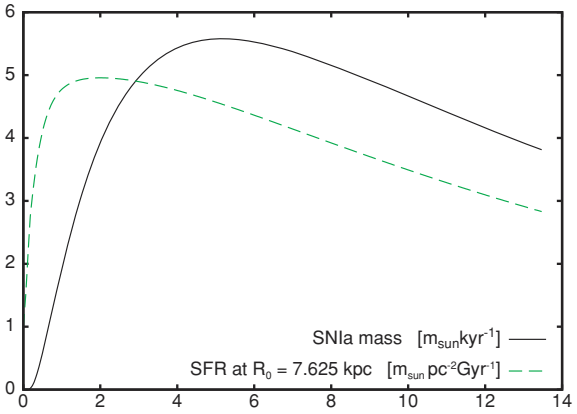

Figure 1. The rate of mass injection by SNIa in the standard model (solid black line) versus time. The broken green line gives the SFR in the solar annulus.

in Fig. 1 shows for the best-fitting model the mass-return rate as a function of time, while the green dashed curve shows the SFR at the solar radius.

2.4 Inflow

It is generally agreed that viable models of galactic chemical evolution require the disc to be constantly fed with gas from intergalactic space; inflow resolves several serious problems, including (i) the appearance of too many low-metallicity stars near the Sun (the 'G-dwarf problem'; e.g. Pagel 1997), (ii) excessive metallicity of the current ISM and (iii) an unrealistically low abundance of deuterium in the current ISM (Linsky et al. 2006). Moreover, both the short time-scale for the current ISM to be consumed by star formation and direct manifestations of infalling gas (Sancisi et al. 2008) argue strongly for the existence of infall. Unfortunately, many aspects of infall are extremely uncertain. We find that the predictions of our models depend sensitively on how these uncertainties are resolved, so to the extent that other aspects of our models have sound foundations, they can usefully constrain the nature of infall.

In principle, the rate and radial distribution of infall are determined by cosmology. For example, Naab & Ostriker (2006) infer it by assuming that the disc scalelength grows in parallel with the cosmic scale, while Colavitti et al. (2008) derive the global rate from *N*-body simulations. At this stage, we feel that cosmological simulations are beset by too many uncertainties to deliver even a secure global infall rate, never mind the radial distribution of infall. In particular, the extent of angular-momentum exchange between baryons and dark matter is controversial, as are the extent to which gas is accreted from cold infall rather than a hot corona. Moreover, nothing is known with any confidence about the dynamics of the corona.

For want of clear inputs from cosmology, we have sought a flexible parametrization of infall. First, we parametrize the global infall rate, and then the radial distribution of infall.

2.4.1 *Infall rate*

We have investigated two approaches to the determination of the infall rate. The first starts with a quantity of gas ($8 \times 10^9\,\mathrm{M}_\odot$) and feeds gas into it at a rate

$$\dot{M} = \frac{M_1}{b_1}\mathrm{e}^{-t/b_1} + \frac{M_2}{b_2}\mathrm{e}^{-t/b_2}. \qquad (6)$$

Here, $b_1 \simeq 0.3$ Gyr is a short time-scale that ensures that the SFR peaks early on, while $b_2 \simeq 14$ Gyr is a long time-scale associated with sustained star formation in the thin disc. We adopt $M_1 \simeq 4.5 \times 10^9\,\mathrm{M}_\odot$ and choose M_2 such that after 12 Gyr the second exponential has delivered $2.6 \times 10^{10}\,\mathrm{M}_\odot$.

In an alternative scheme, the gas mass within the disc is determined a priori and infall is assumed to be available to maintain the gas mass at its prescribed level. We have investigated schemes in which the gas mass declines exponentially with time, but focused on models in which it is held constant at $8.4 \times 10^9\,\mathrm{M}_\odot$; models in which the gas mass declines exponentially produce very similar results to models in which the infall rate declines exponentially.

2.4.2 *Distribution of infall*

We know even less about the radial distribution of the infalling gas than we do about the global infall rate. In fact, our only constraint is that the stellar disc has an approximately exponential surface density now, and was probably exponential at earlier times too. Besides the star formation law, the structure of the stellar disc depends on both the radial distribution of infall and gas flows within the disc, and a disc that is consistent with observations will not be formed if either the radial infall profile or the internal gas flow is fixed without regard to the other process. Consequently, the requirement that only observationally acceptable discs be produced requires one to develop a parametrization that couples infall and flow in a possibly unphysical way. The scheme we have developed involves such an unphysical coupling – this is the price one pays for a scheme that allows one to explore as economically but fully as possible a range of infall profiles and internal flows that are consistent with the known radial structure of the disc.

We start from the assumption that the surface density of gas is at all times exponential, $\Sigma_\mathrm{g}(R) \propto \mathrm{e}^{-R/R_\mathrm{d}}$, where $R_\mathrm{d} = 3.5$ kpc is chosen such that with the star formation law adopted above, the inner stellar disc acquires a scalelength $R_* = R_\mathrm{d}/1.4 = 2.5$ kpc similar to that determined from star counts (Robin et al. 2003; Juric et al. 2008). Our value for the scalelength of the gas disc is in good agreement with the value measured by Kalberla & Dedes (2008): 3.75 kpc. Note that we assume not only that the stellar disc is exponential, but also that its scalelength is unchanging. Hence, we are assuming that the disc forms simultaneously at all radii, rather than 'inside-out'. The remarkably large age estimated for the solar neighbourhood (at $R = 3R_*$) suggests simultaneous formation (Aumer & Binney 2008, and references therein). However, our work could be readily generalized to inside-out growth by making R_d a specified function of time (e.g. Naab & Ostriker 2006), but we reserve this extension for a later paper.

Our scheme for parametrizing infall and flow depends on two parameters, f_A and f_B, and is easiest to explain by considering first the limiting cases in which one parameter vanishes.

Either of the algorithms of the last section specifies what the total gas mass should be at the start of a time-step: this is either the prescribed constant or, when equation (6) is used, it is the mass in the disc at the end of the previous time-step plus the amount that falls in during the most recent time-step. Hence, the mass that should be in each annulus at the start of a time-step follows from the assumed exponential profile of the gas disc. Subtracting from this the mass that was present after the previous time-step, we calculate the need, i.e. the amount of gas that has to be added, of the *i*th annulus ΔM_i.

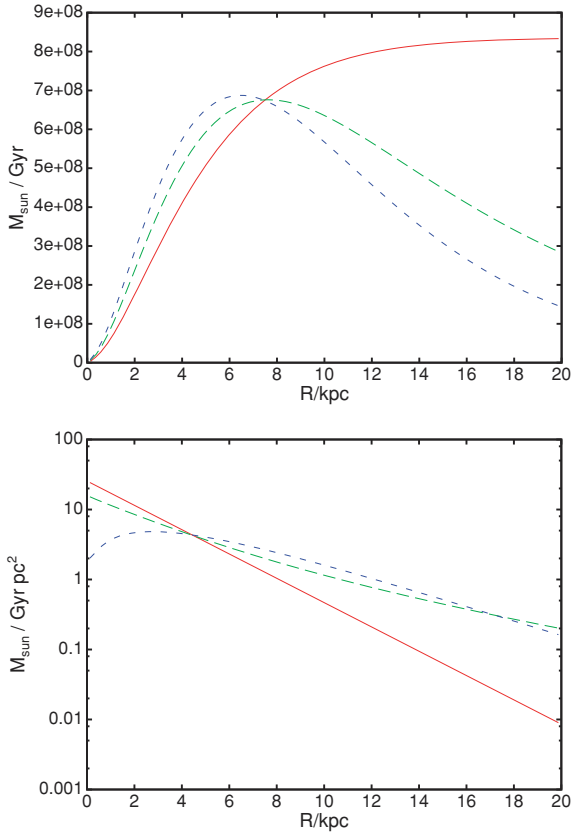

Figure 2. Upper panel: the rate of flow of gas over the circle of radius R induced by infall Scheme A with $f_{\rm A} = 0.6$ (red curve), infall Scheme B with $f_{\rm B} = 0.05$ (blue short dashed curve) and infall Scheme AB with $f_{\rm A} = 0.35$ and $f_{\rm B} = 0.025$ (green long dashed curve; the standard model). Lower panel: the corresponding rates of accretion from the IGM per unit area of the disc.

We fill annuli up with gas in sequence, starting with the innermost ring 0. When $f_{\rm B} = 0$ ('Scheme A'), this annulus receives $f_{\rm A}\Delta M_0$ from the IGM, and grabs the balance, $(1 - f_{\rm A})\Delta M_0$, from annulus 1, where $f_{\rm A} \simeq 0.2$ is a parameter of the model. Annulus 1 receives $f_{\rm A}\Delta M_1$ from the IGM, and grabs the balance of its requirement, $(1 - f_{\rm A})(\Delta M_1 + \Delta M_0)$, from annulus 2. The updating of every annulus proceeds similarly, until the last annulus is reached, which covers its entire need from the IGM. The characteristic of this 'Scheme A' is the development of a large flux of gas through the outer rings – an example is given by the full red curve in the upper panel of Fig. 2. This flux transports inwards metals synthesized in these rings and tends to deposit them at intermediate radii, where the inwards flux is diminishing.

When $f_{\rm A} = 0$ ('Scheme B'), annulus 0 obtains $f_{\rm B}\ \Delta M_0$ from the IGM and the rest from annulus 1. Annulus 1 now obtains $f_{\rm B}[\Delta M_1 + (1 - f_{\rm B})\Delta M_0]$ from the IGM, and so on to the outermost ring, which is again entirely fed by the IGM. The short dashed blue curve in the upper panel of Fig. 2 shows a typical example of a mass flow through the disc with Scheme B. Whereas the flow generated by Scheme A (red curve) increases monotonically from the centre, the Scheme-B flow rises quickly with galactocentric distance R near the centre but then peaks at $R \simeq 5$ kpc. In the outer region in which the inflow is small, the metallicity forms a plateau. The extent of this plateau is controlled by $f_{\rm B}$: the larger $f_{\rm B}$, the smaller the radius at which the inflow rate peaks and the further in the metallicity plateau extends.

In either of these schemes, a fixed fraction of each annulus's need is taken from the IGM, but the definition of 'need' is different in the two schemes: in Scheme B, it includes the gas that was taken from it by its inner neighbour, and in Scheme A it does not. In Scheme A, only a fixed fraction of the local need is provided by the IGM, so the flow F_r in the disc continuously builds up through the disc. In Scheme B, by contrast, a part of the flow required in Scheme A is met by additional accretion. Consequently, if one wrote an equation for $\mathrm{d}F_r/\mathrm{d}r$, a term $-(f_B\Delta r)F_r$ would appear, where $\Delta r = 0.25$ kpc is the width of annuli, and this term drives exponential decay of F_r. Scheme A enhances the metallicity of the middle section of the disc and causes the metallicity gradient to be steepest towards the outside of the disc; Scheme B enhances the metallicity of the inner disc and flattens the gradient at large radii.

In Scheme A, if $f_{\rm A}$ is set too low, the flux of gas through the outer annuli becomes implausibly large in relation to the mass of gas that is in these annuli, and radial flow velocities $v_R \gtrsim 20\,\mathrm{km\,s^{-1}}$ are predicted. In Scheme B, $f_{\rm B}$ can be quite small because, although the flow of gas through the disc builds up more quickly at small radii, it peaks at a few kiloparsec and then declines to small values in the outer disc. If either $f_{\rm A}$ or $f_{\rm B}$ is large, the flow through the disc becomes small and the metallicity of the solar neighbourhood becomes unrealistically large through the accumulation of metals created at the solar radius and beyond.

Satisfactory fits to the data can be obtained only when both $f_{\rm A}$ and $f_{\rm B}$ are non-zero. In this 'Scheme AB' annulus 0 receives a mass $(f_{\rm A} + f_{\rm B})\Delta M_0$ from the IGM and grabs the balance $M_{01} = (1 - f_{\rm A} - f_{\rm B})\Delta M_0$ from annulus 1. Annulus 1 receives a mass $f_{\rm A}\Delta M_1 + f_{\rm B}(\Delta M_1 + M_{01})$ from the IGM and grabs the balance of its requirement from annulus 2, and so on. Note that the radial flow profile in Scheme AB is not simply the sum of the corresponding profiles for Schemes A and B used alone. The green curve in the upper panel of Fig. 2 shows the radial flow profile obtained with Scheme AB with the parameters of the standard model. In this model, the radial velocity of disc gas currently rises roughly linearly from zero at the centre to $1.3\,\mathrm{km\,s^{-1}}$ at the Sun. Beyond the Sun, a plot of radial velocity versus radius gradually steepens to reach $5\,\mathrm{km\,s^{-1}}$ at the edge of the disc.

For each accretion scheme, the lower panel of Fig. 2 shows the corresponding radial distribution of accretion from the IGM.

2.4.3 *Metallicity of the IGM*

We have to prescribe the metallicity and α-enhancement of gas taken from the IGM. It is far from clear how this should be done.

Quasar absorption line studies reveal an early build up of heavy elements in the IGM (Pettini et al. 2003). Moreover, the handful of high-velocity clouds for which metallicities have been measured have heavy-element abundances of the order of a tenth solar (van Woerden & Wakker 2004). Finally, the metallicities of the most metal-poor thick-disc stars are similar to the metallicities of the most metal-rich halo stars, which suggests that the early disc was pre-enriched by pregalactic and halo stars. We assume that throughout the simulation accreted gas has metallicity $Z = 0.1\,\mathrm{Z}_\odot$.

Given that the thick disc is α-enhanced (Venn et al. 2004), it is clear that when disc formation starts, infalling gas must be α-enhanced. It is natural that this enhancement should decline with time as Fe from Type Ia SNe finds its way into the IGM. Indeed, in addition to gas that flows out in the Galactic wind (Bland-Hawthorn & Cohen 2003), Type Ia SNe in dwarf spheroidal galaxies will have contributed their Fe to the local IGM, and if the Magellanic Stream

is made of gas torn from the SMC, it will have been enriched with Fe from SNe in the SMC. Thus, we expect the metallicity and α-enhancement of the IGM to be time-dependent and governed by the chemical evolution histories of galaxies.

These considerations suggest making the α-enhancement of the IGM reflect that of an outer annulus of the Galaxy; the chemical evolution of this ring acts as a proxy for the combined chemical evolution of the many contributors to the chemical evolution of the IGM. If the IGM were assumed to mirror the outermost ring, its α-enhancement would remain extremely low because this annulus takes all its gas from the IGM, and passes what few heavy elements it synthesizes inwards. Hence, the IGM must mirror an outer annulus but not the outermost. In our models, the α-enhancement of the IGM mirrors the annulus with radius $R = 12.125$ kpc. Since yields of α-elements decline with increasing metallicity, the outer disc should be α-enhanced.

2.5 Churning

Transient spiral arms cause both stars and gas to be exchanged between annuli in the vicinity of the corotation resonance. Such exchanges automatically conserve both angular momentum and mass. Since these exchanges are driven by spiral structure, in which hot and extraplanar gas is not expected to participate, churning is confined to stars and cold gas. We restrict exchanges to adjacent rings but allow two exchanges per time-step, so within a time-step second-nearest neighbouring rings exchange mass.

Further studies of spiral structure in high-quality N-body simulations are required to determine how the probability of a star migrating varies across the disc. In the absence of such studies, the following dimensional argument suggests what the answer might be. Consider the probability $P_{\rm ex}$ that in a characteristic dynamical time κ^{-1} (where κ is the local epicycle frequency) a star is involved in a resonant exchange across corotation. It is natural that a process dependent on gravitational self-energy in the disc should scale with the square of the surface density. Toomre's $Q = \sigma\kappa/\pi G\Sigma$, where σ is the radial velocity dispersion, is a dimensionless variable, so we conjecture that $P_{\rm ex} \propto 1/Q^2$. Our grid is uniform in R whereas an exchange across corotation changes R by an order of the most unstable wavelength $\lambda_{\rm crit} = \sigma Q/\kappa$. The number of swaps between rings required to wander a distance $\lambda_{\rm crit}$ scales as $\lambda^2_{\rm crit}$. Moreover, the number of ring-swaps in time κ^{-1} scales as κ^{-1}, so the ring-swap probability per time-step $P_{\rm ring}$ should be $\lambda^2_{\rm crit}\kappa$ times $P_{\rm ex}$. This argument yields $P_{\rm ring} \propto \sigma^2/\kappa$. In realistic cases $\sigma^2 \propto \Sigma$ and $\kappa \propto R$, so $P_{\rm ring} \propto \Sigma R \propto M$, the mass of a ring. This argument suggests that we take the probability p_{ij} that in a given half-time-step a star or gas cloud in the ith annulus is transferred to the jth annulus to be

$$p_{ij} = \begin{cases} k_{\rm ch} M_j/M_{\rm max} & \text{for } j = i \pm 1 \\ 0 & \text{otherwise,} \end{cases} \tag{7}$$

where M_j is the mass in cold gas and stars in the jth annulus and $M_{\rm max} = \max_j(M_j)$. This rule ensures that the mass transferring outwards from the ith annulus is proportional to $M_i M_{i+1}$, and an equal mass transfers inwards, ensuring that angular momentum is conserved. The constant $k_{\rm ch}$ is the largest transition probability for any annulus in a given time-step. It is treated as a free parameter to be fitted to the data.

The procedure for distributing the metals released by a population of stars born in annulus i is as follows. The probability that a star born in annulus i at time-step m is found to be in annulus j at time-step n is equal to the ijth element of the product matrix $\mathbf{p}_m\mathbf{p}_{m+1} \times \cdots \mathbf{p}_n$. In practice, we recompute $\mathbf{p}$ only every fifth timestep and approximate $\mathbf{p}_m \times \cdots \mathbf{p}_{m+4}$ by $\mathbf{p}^5_m$. Fig. 3 shows the extent to which the guiding centres of stars are changed over the lifetime of the Galaxy when $k_{\rm ch} = 0.25$.

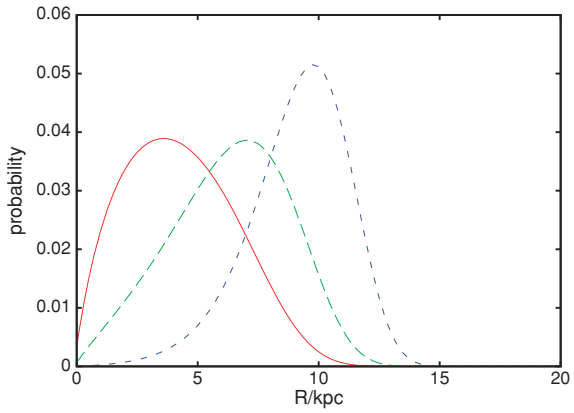

Figure 3. The radial distribution of the guiding centres of 12 Gyr old stars that were born at 5 (red), 7.6 (green, long dashed) and 10 kpc (blue, short dashed) when the churning fraction $k_{\rm ch} = 0.25$.

2.6 Blurring

In addition to changing their guiding-centre radii through the churning process, stars oscillate around their guiding centres with steadily increasing amplitudes. Consequently, stars spend time away from their guiding-centre radii. For simplicity, we assume in this section that the circular speed $v_{\rm c}$ is independent of radius and that the vertical motion can be ignored because it decouples from motion in the plane.

The fraction of its time that the orbit with energy and angular momentum E, L spends in a radial interval $(R, R + {\rm d}R)$ is

$${\rm d}p = \frac{{\rm d}t}{T} = \frac{1}{T}\frac{{\rm d}R}{v_R} = \frac{\Omega_{\rm R}}{\pi}\frac{{\rm d}R}{\sqrt{2(E - \Phi_{\rm eff})}}, \tag{8}$$

where $T \equiv \pi/\Omega_{\rm R}$ is the half period and $\Phi_{\rm eff}(R, L) \equiv \Phi(R) + L^2/2R^2$ is the effective potential. We need to average this over all stars with given L. These stars have some distribution over the energy $E = \frac{1}{2}v_R^2 + \Phi_{\rm eff}$. It is expedient to decompose E into the energy $\Phi_{\rm c}(L) \equiv \Phi(R_{\rm c}) + L^2/2R_{\rm c}^2$ of the circular orbit (with radius $R_{\rm c}$) of angular momentum L and the random energy $\mathcal{E} \equiv E - \Phi_{\rm c}$. Following Shu (1969), we take the distribution function (DF) to be

$$f(\mathcal{E}, L) = \frac{F(L)}{\sigma^2}{\rm e}^{-\mathcal{E}/\sigma^2}, \tag{9}$$

where $F(L)$ is a function to be determined. The DF (9) ensures that the radial velocity dispersion is approximately (but not exactly) σ. Normalizing f such that $\int {\rm d}L\,{\rm d}J_R\, f = 1$, where $J_R(\mathcal{E})$ is the radial action, the probability that a randomly chosen star lies in $(R, R + {\rm d}R)$ is $\int {\rm d}L\,{\rm d}J_R\, f{\rm d}p$. Recalling that ${\rm d}L\,{\rm d}J_R = {\rm d}L\,{\rm d}\mathcal{E}/\Omega_{\rm R}$ and substituting for f and ${\rm d}\,p$, we find that the number of stars in the annulus is

$$\begin{aligned} {\rm d}n(R) &= \int {\rm d}L\,{\rm d}J_R\,(f{\rm d}p) \\ &= \frac{N{\rm d}R}{\pi}\int {\rm d}L\,\frac{F}{\sigma^2}\int_{\Phi_{\rm eff}-\Phi_{\rm c}}^{\infty}{\rm d}\mathcal{E}\,\frac{{\rm e}^{-\mathcal{E}/\sigma^2}}{\sqrt{2(\mathcal{E} + \Phi_{\rm c} - \Phi_{\rm eff})}} \\ &= \frac{N{\rm d}R}{\sqrt{2}\pi}\int {\rm d}L\,\frac{F}{\sigma^2}{\rm e}^{[\Phi_{\rm c}-\Phi_{\rm eff}]/\sigma^2}\int_0^{\infty}{\rm d}x\,\frac{{\rm e}^{-x/\sigma^2}}{\sqrt{x}}, \end{aligned} \tag{10}$$

where N is the total number of stars in the system. The integral over x is simply $\sigma\int {\rm d}t\,{\rm e}^{-t}/\sqrt{t} = \sqrt{\pi}\sigma$. Thus, we can conclude that the

probability per unit area associated with a star of given L is

$$P(R) = \frac{\mathrm{d}n}{N 2\pi R \mathrm{d}R} = \frac{K}{\sigma R} \exp\left[\frac{\Phi_\mathrm{c}(L) - \Phi_\mathrm{eff}(R, L)}{\sigma^2}\right], \quad (11)$$

where K is chosen such that $1 = 2\pi \int \mathrm{d}R\, R P(R)$.

The parameter σ used in these formulae is actually smaller than the rms radial velocity dispersion, which is given by

$$\langle v_R^2 \rangle = \frac{\sqrt{2\pi}}{R\Sigma} \int \mathrm{d}L\, F\sigma \exp\left[(\Phi_\mathrm{c} - \Phi_\mathrm{eff})/\sigma^2\right], \quad (12)$$

where the stellar surface density is

$$\Sigma(R) = \frac{\sqrt{2\pi}}{R} \int \mathrm{d}L\, \frac{F}{\sigma} \exp\left[(\Phi_\mathrm{c} - \Phi_\mathrm{eff})/\sigma^2\right]. \quad (13)$$

For specified radial dependencies of Σ and $\langle v_R^2 \rangle$, equations (12) and (13) can be used to determine the functions $F(L)$ and $\sigma(L)$ (Dehnen 1999). However, in the present application it is not $\Sigma(R)$ that we wish to specify, but the number of stars with guiding centres in each ring:

$$\begin{aligned} \frac{\mathrm{d}N}{\mathrm{d}R_\mathrm{c}} &= v_\mathrm{c} N_\mathrm{tot} \frac{\mathrm{d}N}{\mathrm{d}L} = v_\mathrm{c} \int \mathrm{d}J_R\, f(L, J_R) \\ &= \frac{v_\mathrm{c} F N_\mathrm{tot}}{\sigma^2} \int \frac{\mathrm{d}\mathcal{E}}{\Omega_\mathrm{R}} \mathrm{e}^{-\mathcal{E}/\sigma^2}, \end{aligned} \quad (14)$$

where N_tot is the total number of stars in the disc. We adapt the technique described by Dehnen (1999) for determining $F(L)$ and $\sigma(L)$ from equations (12) and (13) to the determination of these quantities from equations (12) and (14). Specifically, we start from the values of $F(L)$ and $\sigma(L)$ that would hold in the epicycle approximation, when $\Omega_\mathrm{R} = \kappa$ independent of $\mathcal{E}$ and

$$F(L) = \frac{\kappa}{v_\mathrm{c} N_\mathrm{tot}} \frac{\mathrm{d}N}{\mathrm{d}R_\mathrm{c}}. \quad (15)$$

Then, at each L we evaluate $\langle v_R^2 \rangle$ from (12) and multiply σ by the ratio of the desired value to the value just calculated. Then, we re-evaluate F from (14) and repeat until convergence is obtained.

We now address the question of how $\langle v_R^2 \rangle$ should depend on radius. The scaleheights h of galactic discs are found to be largely independent of radius (van der Kruit & Searle 1982), and for $h \ll R$ (when the vertical dynamics can be considered one-dimensional) this finding implies that the vertical velocity dispersion scales with the surface density as $\Sigma^{1/2}$. If the ratio of the vertical and radial velocity dispersions $\sigma_z/\langle v_R^2 \rangle^{1/2}$ is independent of radius, as is often assumed (e.g. Kregel & van der Kruit 2005), then $\langle v_R^2 \rangle \propto \Sigma \propto \mathrm{e}^{-R/R_*}$. In the solar neighbourhood at $R \simeq 3R_*$ the oldest stars have $\sigma_R \gtrsim 40\,\mathrm{km\,s^{-1}}$, so this line of reasoning predicts that $\langle v_R^2 \rangle^{1/2} \gtrsim 180\,\mathrm{km\,s^{-1}}$ in the central regions, which is implausibly large.

Evidently, these naive arguments based on complete decoupling of planar and vertical motions are inadequate for the old disc; we need a DF that treats the third integral properly. Pending the availability of such a DF, we have adopted the assumption that $\langle v_R^2 \rangle \propto \mathrm{e}^{-R/1.5R_*}$, which implies that at R_* the old disc has $\langle v_R^2 \rangle^{1/2} \simeq 85\,\mathrm{km\,s^{-1}}$, which is only slightly lower than the velocity dispersion in the Galactic bulge (Rich et al. 2007).

From Binney, Dehnen & Bertelli (2000) we take the time dependence of $\sqrt{\langle v_R^2 \rangle}(R_0)$ at solar galactocentric distance R_0 to be

$$\sqrt{\langle v_R^2 \rangle}(R_0, t) = \max\left\{10, 38\left(\frac{t + 0.038\,\mathrm{Gyr}}{10.038\,\mathrm{Gyr}}\right)^{0.33}\right\} \mathrm{km\,s^{-1}}, \quad (16)$$

which is consistent with the data of Holmberg et al. (2007).

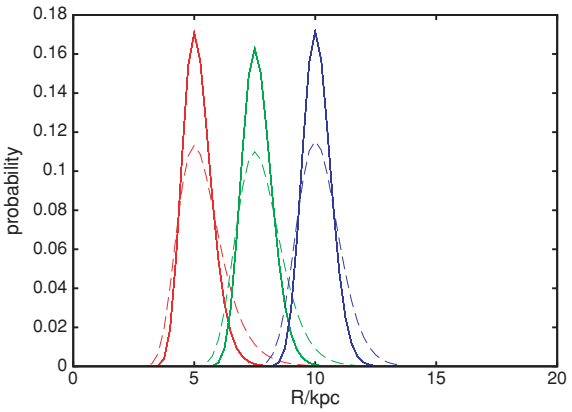

Figure 4. The radial distributions of stars with guiding centres at 5 (red), 7.6 (green) and 10 kpc (blue) when at the Sun $\langle v_R^2 \rangle^{1/2} = 25\,\mathrm{km\,s^{-1}}$ (full curves) and $40\,\mathrm{km\,s^{-1}}$ (dashed curves).

Fig. 4 shows blurring distributions $P(R)$ from equation (11) for three radii (5, 7.6 and 10 kpc) and two values of $\langle v_R^2 \rangle^{1/2}$ at the Sun, namely 25 and $40\,\mathrm{km\,s^{-1}}$.

Note that scatterings by spiral arms and molecular clouds that heat the disc also change the angular momentum of each star and therefore its guiding centre. Hence such scatterings contribute to both churning and blurring.

Since churning moves the guiding centres of the stars themselves, we first apply the churning matrix and apply the blurring matrix afterwards.

2.7 Vertical structure

For comparison with observations of the solar neighbourhood we need to know the vertical distribution of stars near the Sun. We determine this by adopting a relationship between time and vertical velocity dispersion (Binney et al. 2000)

$$\sigma_z(\tau) = \max\left\{4, 25\left(\frac{\tau}{10\,\mathrm{Gyr}}\right)^{0.33}\right\} \mathrm{km\,s^{-1}}. \quad (17)$$

Further assuming that stars of a given age form an isothermal population, their vertical density profile is

$$n(z) \propto \mathrm{e}^{-\Phi(z)/\sigma_z^2}, \quad (18)$$

where $\Phi(z)$ is the difference in the gravitational potential between height z and the plane. This potential is calculated for a model similar to those presented by Dehnen & Binney (1998) but with the thin- and thick-disc scaleheights taken to be 0.3 and 0.9 kpc, the total stellar surface density set to $35.5\,\mathrm{M_\odot\,pc^{-2}}$ with 3/4 of the stellar mass in the thin disc and the gas surface density set to $13.2\,\mathrm{M_\odot\,pc^{-2}}$ in conformity with Flynn et al. (2006) and Juric et al. (2008). The disc scalelength is taken to be $R_\mathrm{d} = 2.5$ kpc (Robin et al. 2003) and the dark halo density is set such that $v_\mathrm{c}(R_0) = 220\,\mathrm{km\,s^{-1}}$.

3 THE STANDARD MODEL

We now describe the properties of our standard model as a preliminary to explain how these properties depend on the input assumptions and the values of the various parameters. In the standard model, the accretion rate is given by equation (6); the values of the parameters for this model are given in Table 1.

The red dashed curve in Fig. 5 shows the current metallicity Z of the ISM as a function of radius. There is quite a steep outwards

Table 1. Parameters of the standard model. The infall rate is given by equation (6). The larger value of $f_{\rm eject}$ applies at $R < 3.5$ kpc.

Parameter	Meaning	Impact	Value
$\Sigma_{\rm crit}$	Kennicutt's threshold surface density	Limited impact	0
M_0	Initial gas mass	Affects only $N(Z)$ at $[Z/H] < -0.7$; from Hess diagram	$3.0 \times 10^9\,M_\odot$
M_1	Early infall mass	Affects only $N(Z)$ at $[Z/H] < -0.7$; from Hess diagram	$4.5 \times 10^9\,M_\odot$
M_2	Long time-scale infall mass to 12 Gyr	Fixed by present mass	$2.9 \times 10^{10}\,M_\odot$
b_1	Early infall time-scale	Affects only $N(Z)$ at $[Z/H] < -0.7$; from Hess diagram	0.3 Gyr
b_2	Long infall time-scale	Limited impact; estimated from Hess diagram and other work	14 Gyr
$f_{\rm A}$	Scheme A fraction of gas from IGM	Free parameter	0.36
$f_{\rm B}$	Scheme B fraction of gas from IGM	Free parameter fixed by local gradient	0.025
$k_{\rm ch}$	Churning amplitude	Free parameter	0.35
t_0	Delay before first Type Ia SNe	Taken from literature	0.15 Gyr
k^{-1}	Time-scale for decay of Type Ia SNe	Taken from literature	1.5 Gyr
$f_{\rm eject}$	Fraction of ejecta lost to Galaxy	Small impact; mainly affects metallicity scale	$0.15 - 0.04$
$f_{\rm direct}$	Fraction of ejecta to cold ISM	Small impact limited to $[Z/H] < -0.7$	0.01
$t_{\rm cool}$	Cooling time of warm gas	Fixed by present mass of warm gas	1.2 Gyr
$M_{\rm warm}$	Initial warm gas mass	Impact limited to $N(Z)$ at $[Z/H] < -0.7$	$5 \times 10^8\,M_\odot$
$Z_{\rm IGM}$	Metallicity of the IGM	Limited to $R > 12$ kpc; taken from literature	$0.1\,Z_\odot$

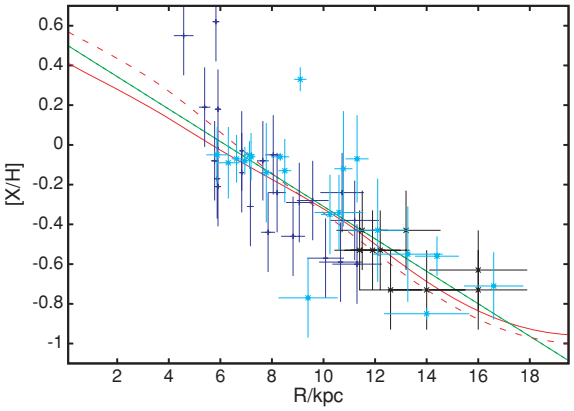

Figure 5. The metallicities of the current ISM in the standard model, [*Z*/H] (red dashed curve) and [O/H] (red full curve), as functions of galactocentric radius. Also measurements of the metallicities of H II regions by Shaver et al. (1983) (dark blue), Vilchez & Esteban (1996) (black crosses) and Rolleston et al. (2000) (light blue crosses). The green line shows the linear least-squares fit to the measurements: it has a slope of $-0.082\,{\rm dex\,kpc^{-1}}$. The data points have been updated and rescaled to $R_0 = 7.5$ kpc as described in the text. Where necessary points have been shifted vertically by -8.93 to put them on the solar scale.

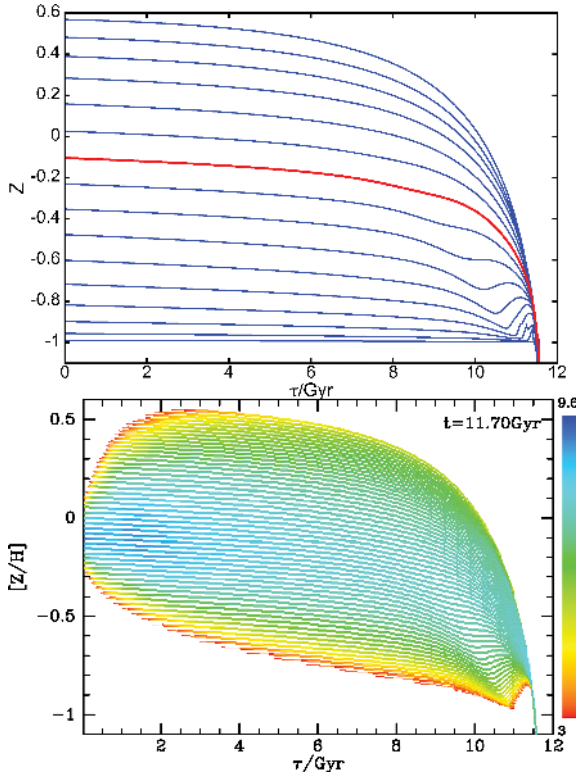

Figure 6. Upper panel: the metallicity of the cold ISM in each annulus as a function of lookback time showing each fifth ring. The curve for the solar annulus is red. Lower panel: the present density of solar-neighbourhood stars in the age–metallicity diagram. The colours encode the logarithm of the density of stars.

decline in metallicity, the gradient in the vicinity of the Sun being of the order of $-0.11\,{\rm dex\,kpc^{-1}}$. The solid red curve shows that [O/H] falls less steeply with R than does [*Z*/H], having a gradient near the Sun $\sim -0.083\,{\rm dex\,kpc^{-1}}$. The shallower gradient in oxygen reflects our use of metallicity-dependent yields. Although shallower gradients are generally cited (e.g. Rolleston et al. 2000), the data points in the figure are consistent with the model. The data derive from Shaver et al. (1983) who assumed $R_0 = 10$ kpc and from Vilchez & Esteban (1996) and Rolleston et al. (2000), who assumed $R_0 = 8.5$ kpc. To plot these data on a consistent scale with $R_0 = 7.5$ kpc, we have when possible recalculated the galactocentric distances from the heliocentric distances, taking the latter from Kharchenko et al. (2005) or Loktin & Beshenov (2003) when possible. For some of the points in Vilchez & Esteban (1996) and Rolleston et al. (2000), heliocentric distances were not available, so we simply reduced the cited galactocentric distance by 1 kpc. The green line in Fig. 5 is the linear least-squares fit to the data; its slope is $-0.082\,{\rm dex\,kpc^{-1}}$. Our gradient in [O/H] lies within the range of frequently occurring values in table 4 of Vila-Costas & Edmunds (1992), who assembled data for 30 disc galaxies.

The upper panel in Fig. 6 shows the evolution of Z for the cold ISM in a number of annuli – the solar annulus is coloured red. The smaller the radius of an annulus, the higher its curve lies in this plot because chemical evolution proceeds fastest and furthest at small radii. At small radii, the metallicity of the cold ISM continues to increase throughout the life of the Galaxy, whereas at $R \gtrsim R_0$ kpc, Z peaks at a time that moves earlier and earlier as one moves out, and

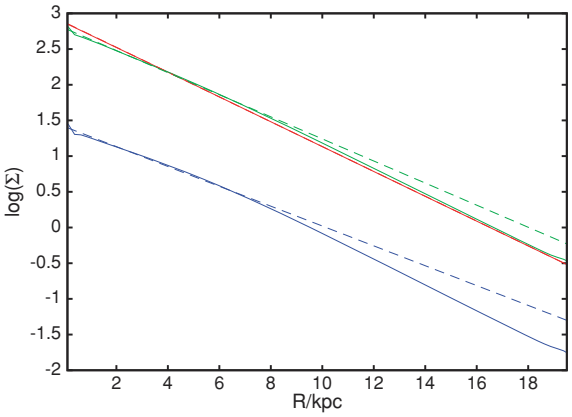

Figure 7. Full green curve: the surface density of the stellar disc at 11.7 Gyr. Broken green line: exponential fit to the inner part of this curve. Red curve: the surface density if stars remained where they were born. Blue curve: surface density contributed by stars born in the first 0.8 Gyr. Broken blue line: linear fit to this curve.

declines briefly before flattening out. This phenomenon reflects a combination of dilution by infalling metal-poor gas and the inwards advection of metals by the flow through the disc.

The lower panel in Fig. 6 shows the corresponding present-day metallicity distribution of solar-neighbourhood stars. Although this is the distribution of stars currently in the solar annulus, it is clearly made up of a series of curves, one for each annulus in the model. The curves for interior annuli go from green to yellow as one goes forward in time, reflecting the fact that relatively recently formed stars are much less likely to have moved a large radial distance than older stars. Similarly, in the bottom part of the figure the colours go from blue to green to yellow as one moves towards the time axis, because then one is moving over curves for larger and larger radii, where both the SFR and the probability of scattering in to the solar radius are low. Hence, regardless of stellar age, most solar-neighbourhood stars have Z in a comparatively narrow range centred on $[Z/\mathrm{H}] \simeq -0.1$.

The full green curve in Fig. 7 shows the surface density of the stellar disc at 11.7 Gyr, which is roughly exponential. The red points show what the surface density would be if stars remained at their radii of birth. By construction, this forms an exponential disc with a scalelength of 2.5 kpc. The broken green line shows that at $R < R_0$ the disc approximates an exponential with a larger scalelength $\sim$2.8 kpc. The blue curve shows the surface density contributed by stars formed in the first 0.8 Gyr, which will be α-enhanced. This distribution deviates more strongly from an exponential because radial migration is most important for old stars. Fitting an exponential to this curve at $R < R_0$ yields a scalelength 3.1 kpc.

Fig. 8 reveals that thin- and thick-disc components can be identified within this overall envelope: the upper panel shows that the vertical stellar density profile at the Sun is not exponential but can be fitted by a sum of two exponentials. There is significant latitude in these fits and the fraction of stars that is assigned to each component varies with their scalelengths. For comparison with recent results of Juric et al. (2008), we present a fit with their value for the local thick-disc fraction of 13 per cent. This yielded scaleheights of $h_1 = 335$ pc and $h_2 = 853$ pc, very well in the range of their results. Note that the double-exponential density structure is *not* caused by any peculiarity in star formation history, like a peak in early star formation, but is a consequence radial mixing combined with the given vertical force field. However, precise characterization of the

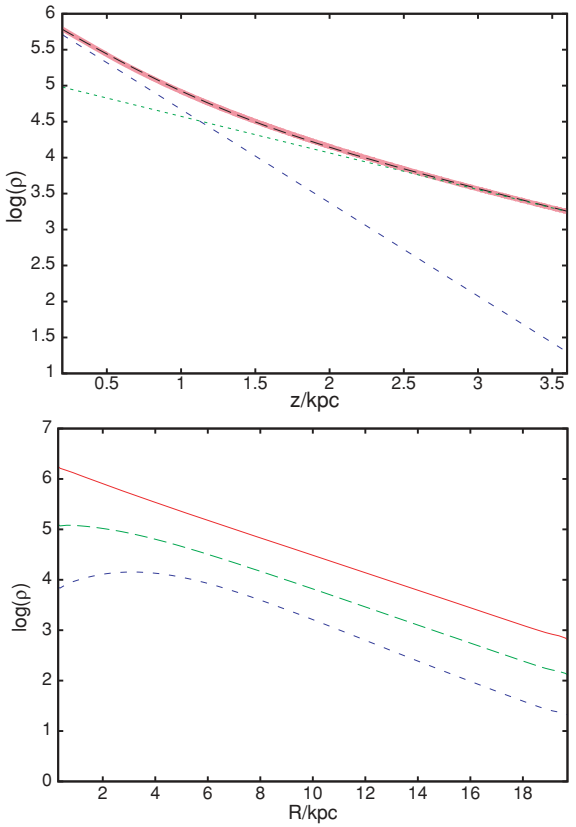

Figure 8. Upper panel: the volume density of stars at $R = 7.6$ kpc as a function of height (red), a fit (black dashed) and its decomposition into thin and thick components. Lower panel: the volume density of stars at the current epoch at $z = 0$ (red), $z = 0.75$ kpc (green dashed) and $z = 1.5$ kpc (blue short dashed).

vertical structure must await dynamical models that employ a more accurate form of the third integral of galaxy dynamics.

The lower panel of Fig. 8 shows that at $z = 1.5$ kpc (where the thick disc is dominant) the stellar distribution is less centrally concentrated than it is in the plane; if one were to fit an exponential profile to the stellar density at $z = 1.5$ kpc for $R < 10$ kpc, the scalelength fitted would be larger than that appropriate in the plane. Just this effect is evident in fig. 16 of Juric et al. (2008).

Fig. 9 shows the predicted distribution of solar-neighbourhood stars in the ([O/Fe], [Fe/H]) plane when a sample is assembled using the GCS selection function described in Section 4. Two ridge lines are evident: at top left of the figure a population starts that stays at $[\mathrm{O/Fe}] \simeq 0.6$ until $[\mathrm{Fe/H}] \simeq -0.75$ and then turns down towards $(0, 0)$, while a second larger population starts at about $(-0.75, 0.25)$ and falls towards $(0.2, -0.05)$. This arrangement of points is very similar to that seen in fig. 2 of Venn et al. (2004). The upper ridge line is associated with the thick disc, and the lower ridge line with the thin disc. In the Appendix, we show that such bimodal distributions in [O/Fe] are a natural consequence of the standard assumptions about SFRs and metal enrichment that we have made. The structure is *not* a product of the double-exponential nature of the standard model's infall law; the model with a constant gas mass displays exactly the same structure. Breaks in the Galaxy's star formation history (Chiappinin et al. 1997) and accretion events (Bensby et al. 2005) have been hypothesized to account for the dichotomy between the thin and thick discs. Our models reproduce the dichotomy without a break or other catastrophic event in our model's star formation

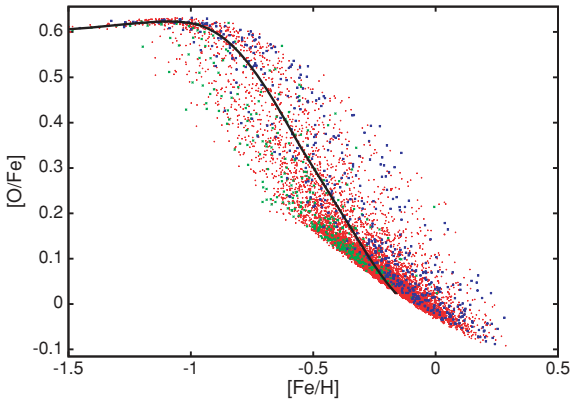

Figure 9. The predicted distribution of solar-neighbourhood stars in the ([Fe/H], [O/Fe]) plane. The sample is obtained by using the selection function of the GCS survey as described in Section 4. The colours of points depend on the star's azimuthal velocity: $v_\phi < 179\,\mathrm{km\,s^{-1}}$ blue; $179 < v_\phi/\,\mathrm{km\,s^{-1}} < 244$ red; $v_\phi > 244\,\mathrm{km\,s^{-1}}$ green. The black curve shows the trajectory of the solar annulus.

history. When comparing Fig. 9 with similar plots for observational samples, it is important to bear in mind differences in selection functions: Fig. 9 is for a kinematically unbiased sample, while most similar observational plots are for samples that are kinematically biased in favour of 'thick-disc' stars.

The full curve in Fig. 9 shows the trajectory of the solar-neighbourhood ISM. At low [Fe/H], this runs along the ridge line of the thick disc, and it finishes on the ridge line of the thin disc, but it is distinct from both ridge lines. The sharp distinction between this curve and the ridge line of the thin disc makes it very clear that the latter is formed through the migration of stars into the solar neighbourhood, *not* through the chemical evolution of the solar neighbourhood itself. In many previous studies, it has been assumed that the ridge line of the thin disc traces the historical evolution of the local ISM. Fig. 9 shows that this assumption could be wrong and that inferences regarding the past infall and SFRs that are based on this assumption are not to be trusted.

In Fig. 9, the points are colour coded by their angular momenta/guiding centres: blue points are for $v_\phi < 179\,\mathrm{km\,s^{-1}}$ ($R_\mathrm{g} < 0.81R_0$), red points are for $179\,\mathrm{km\,s^{-1}} \le v_\phi \le 244\,\mathrm{km\,s^{-1}}$ and green points are for $v_\phi > 244\,\mathrm{km\,s^{-1}}$ ($R_\mathrm{g} > 1.1R_0$). At the low-metallicity end of the thin-disc ridge line, many points are green and few blue, while at the high-metallicity end the reverse is true. Thus, low-metallicity thin-disc stars tend to have guiding centres $R_\mathrm{g} > R_0$, while high-metallicity stars have $R_\mathrm{g} < R_0$. Haywood (2008) has noted the same metallicity–velocity correlations in samples of nearby stars. The thick disc contains stars from all three radial ranges, but stars with small R_g (blue) are most prominent at higher [Fe/H].

Fig. 10 shows the distribution of stars in the $([Z/\mathrm{H}], v_\phi)$ plane: the upper panel is for the GCS stars and the lower panel is for the standard model. In both the panels, the highest density of stars lies near $(0, 220\,\mathrm{km\,s^{-1}})$ and the upper edge of the distribution rises as one moves to lower metallicities. The metallicity gradient in the disc leads to the main cluster of stars sloping downwards to the right. A significant difference between the two panels is that in the upper panel there are more stars in the lower-left region. This population is very much more prominent in fig. 5 of Haywood (2008), where a band of points runs from small v_ϕ and $[Z/\mathrm{H}]$ up towards the main cluster. This band is made up of halo and thick-disc stars that are selected for in the samples from which Haywood drew data. The

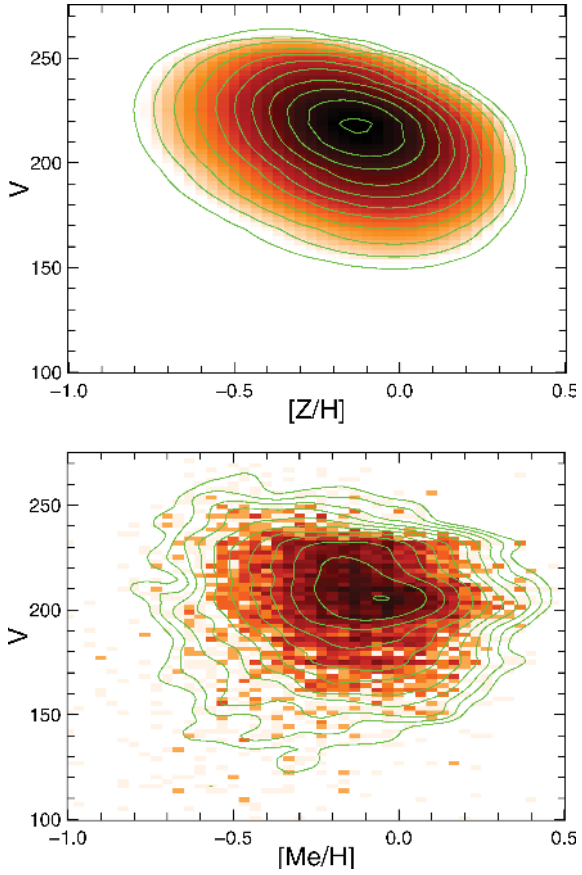

Figure 10. Upper panel: the distribution of GCS stars in the $([Z/\mathrm{H}], v_\phi)$ plane. Lower panel: the prediction of the standard model. Colours and contours reflect the density on a logarithmic scale with a 0.2 dex spacing for contours.

other difference between Haywood's fig. 5 and the lower panel of Fig. 10 is that Haywood's main clump has a slightly less pronounced slope down to the right. It is likely that errors in the measurements of [Fe/H] have moderated this slope. The GCS distribution shown in the upper panel of Fig. 10 is (especially on the high-metallicity side) dominated by overdensities around the rotational velocities of well-known stellar streams (e.g. the Hercules stream; Dehnen 1998). This pattern overlays the general downwards slope. The model accounts well for the steeper edge of the density distribution at high rotational velocities, which is the combined effect of lower inwards blurring and lower stellar densities from outer rings.

The top panel of Fig. 11 shows that the stellar metallicity distribution is less centrally concentrated than that of the cold ISM from which stars form. Three factors are responsible for this result. First, the mean metallicity of stars reflects the metallicity of the gas at earlier times, which was lower. This effect is most pronounced at the centre, where the metallicity of the ISM saturates later than further out. Secondly, radial mixing, which flattens abundance gradients, has a bigger impact on stars than gas because stars experience both churning and blurring. Thirdly, the net inflow of gas steepens the abundance gradient in the gas. Holmberg et al. (2007) have estimated the stellar metallicity gradient from the GCS stars. When they select thin-disc stars, they find $-0.09\,\mathrm{dex\,kpc^{-1}}$, but when one excludes stars with $[Z/\mathrm{H}] < -0.7$ (which ensures halo objects are removed), one obtains $-0.11\,\mathrm{dex\,kpc^{-1}}$. The gradient of the dashed red line in Fig. 11 at 7.6 kpc is $0.10\,\mathrm{dex\,kpc^{-1}}$ in excellent agreement with the GCS data.

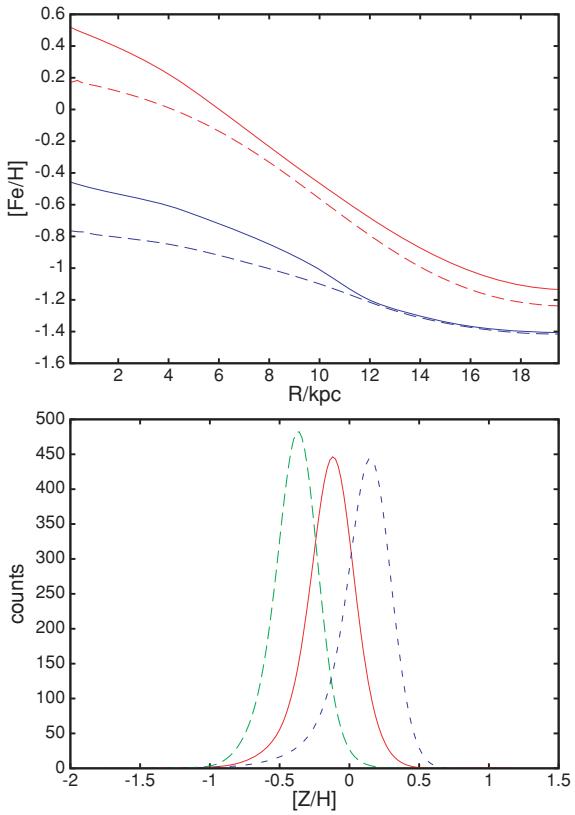

Figure 11. Upper panel: mean metallicities of stars (dashed) and cold ISM (full) as functions of R at the present time (red) and at 1.5 Gyr (blue). Lower panel: the distributions over metallicity of stars currently at $R = 5$ kpc (blue), 7.6 kpc (red) and 10 kpc (green).

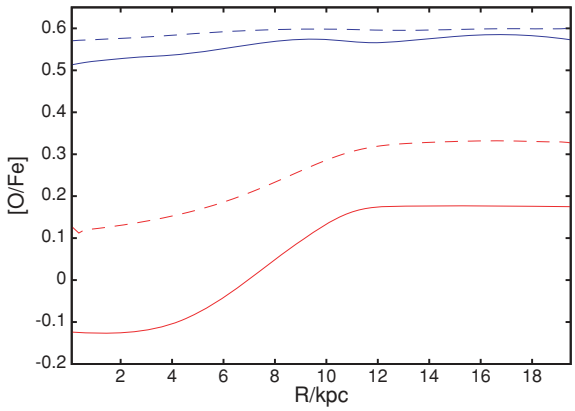

Figure 12. Full lines: [O/Fe] in the cold ISM after 1.5 Gyr (blue) and 12 Gyr (red). Dashed lines: mean [O/Fe] of stars after 1.5 and 12 Gyr.

The lower panel of Fig. 11 shows the breadth of the metallicity distribution at three radii. These distributions have full-width at half maximum around 0.35 dex and are significantly offset to each other by 0.25 dex.

Fig. 12 shows how α-enhancement varies in time and space, in stars and gas. Naturally, [O/Fe] declines with time in both the ISM and in the stellar population, and at a given time is higher in the stars than the gas. [O/Fe] generally increases outwards but at 12 Gyr in both stars and gas it attains a plateau at $R \gtrsim 10$ kpc, with

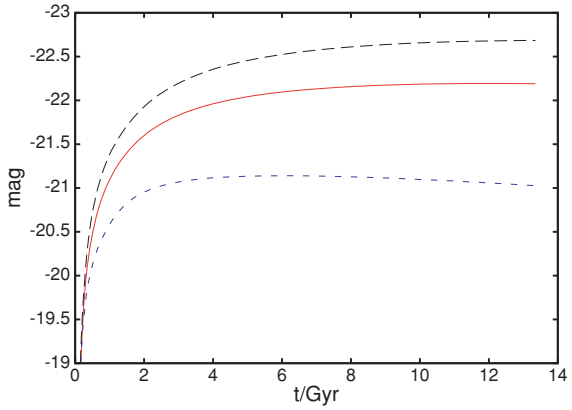

Figure 13. Absolute magnitudes in the B (blue short dashed), R (red) and I (black long dashed) bands as functions of time. No allowance has been made for obscuration.

$[\alpha/\mathrm{H}] \sim 0.2$ in the gas. The existence of the plateau is a consequence of the rule that in the IGM [O/H] is the current value in the disc at $R \simeq 12$ kpc; gas with the given α-enhancement rains on the disc at $R \lesssim 20$ kpc, is enriched by supernovae of both types and, a few gigayears later, arrives at $R = 12$ kpc with its original α-enhancement. This level is set by the metallicity-dependent yields we have employed.

Fig. 13 shows the B-, R- and I-band absolute magnitudes of the standard model as functions of time. The B-band luminosity rises quickly to a shallow peak around 5 Gyr, and then commences a very slow decline. Emissions in the R band are almost constant at the present time, while I-band luminosities continue to rise throughout the Galaxy's life because additions to the stock of long-lived stars outweigh deaths of relatively short-lived and predominantly blue stars. In our model, the Galaxy reaches an I-band magnitude of around -22.7 which is exactly the result one would expect for a disc galaxy with a rotation velocity of 220 km s^{-1} (e.g. Pizagno et al. 2005).

Fig. 14 shows the $U - B$ and $B - I$ colours of the disc at $t = 1.5$, 4.5, 8.4 and 12 Gyr. As expected, the disc reddens at a declining rate throughout its life. There is at all times a significant colour gradient between $R = 8$ and 16 kpc that makes the disc's edge about 0.2 mag bluer in $B - I$ than its centre.

Fig. 15 shows that radial migration causes the dependence of velocity dispersion on time for stars that are currently in the solar neighbourhood to differ materially from the acceleration law (17) that determines the time dependence of σ_z for stars that are born at a given radius. The outward migration of stars brings to the solar-neighbourhood stars that carry with them the large velocity dispersions characteristic of their places of birth. The impact that these migrants have on σ_z for stars of a given age increases with age, so at high ages σ_z increases faster than equation (17) predicts. Least-squares fits of $\sigma_z \propto t^\beta$ to the red and green curves in Fig. 15 yield $\beta = 0.53$ and 0.44, respectively. Empirically, the photometrically complete portion of the *Hipparcos* catalogue shows that the best power-law fits to the rate of increase of σ_z yield $\beta \simeq 0.45$ (Just & Jahreiss 2007; Aumer & Binney 2008). From a theoretical standpoint, this result has hitherto been puzzling because the largest exponent that can be obtained from the dynamics of star scattering is 1/3 (Binney & Lacey 1988). Such studies treat the acceleration as a local process. Our result suggests that the conflict between theory and observation is attributable to violation of this assumption.

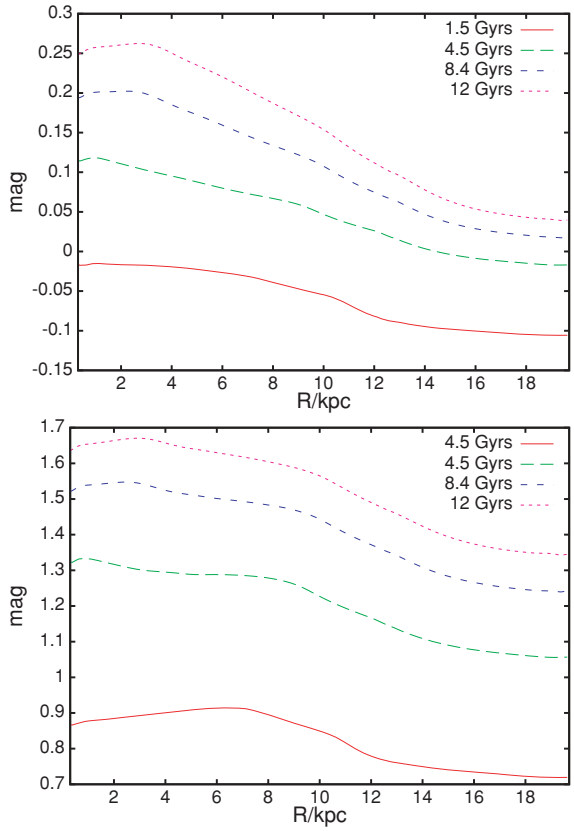

Figure 14. $U - B$ (upper panel) and $B - I$ (lower panel) as functions of radius at $t = 1.5$, 4.5, 8.4 and 12 Gyr. No allowance has been made for obscuration.

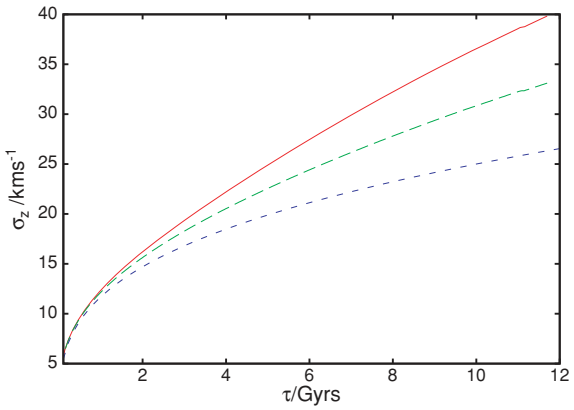

Figure 15. Velocity dispersion of solar-neighbourhood stars as a function of age. Red curve: σ_z for all stars in the solar annulus. Green (long dashed) curve: σ_z for stars within 100 pc of the Sun. Blue (short dashed) curve: σ_z for stars born in the solar annulus.

4 FITTING THE MODEL TO THE SOLAR NEIGHBOURHOOD

A major constraint on the models is provided by comparing the model's predictions with samples of stars observed near the Sun. To make these comparisons, we have to reproduce the selection functions of such samples, which proves a non-trivial job.

The GCS is an important sample, and for each model we calculate the likelihood of this sample. Nordström et al. (2004) obtained Strömgren photometry and radial velocities for a magnitude-limited sample of 16 682 F and G dwarfs, nearly all of which have good *Hipparcos* parallaxes. From the photometry, they estimated metallicities and ages. There has been some debate about the calibration of the metallicities and ages (Haywood 2006; Holmberg et al. 2007; Haywood 2008). Recently, the re-calibrated data from Holmberg et al. (2007) became available, and it is to these data that we have compared our models. We compare their metallicities ([Me/H]) to our $[Z/\mathrm{H}]$ as it is not entirely obvious to what extent alpha enrichment enters into their measurements. Since assigning ages to individual stars is very difficult, we have concentrated on matching the distribution of stars in the $(M_V, T_{\rm eff}, Z)$ space from which ages are derived.

Table 2. Magnitudes defining the Geneva–Copenhagen selection function.

$b-y$	$0.21-0.25$	<0.344	<0.38	<0.42	>0.42
v_1	7.7	7.8	7.8	7.8	8.2
v_2	8.9	8.9	9.3	9.3	9.9

For each metallicity, we construct a volume-limited stellar number density of stars in the $(M_V, T_{\rm eff})$ plane by considering each annulus j, and calculating the fraction of each population in this annulus that will be in the solar neighbourhood. For given absolute magnitude, the probability that a star will enter the sample is

$$W(r_{\rm max}) = \int_0^{r_{\rm max}} \mathrm{d}r\, r^2 \int \mathrm{d}^2\Omega\, n(z), \tag{19}$$

where the space density of stars $n(z)$ is assumed to be plane parallel and given by equation (18).

For the GCS selection function, we use the approximate $b - y$ colour rules from Nordström et al. (2004) – a more sophisticated selection function could in principle be constructed, but it is not possible from the published data. At each colour, the appropriate selection function ϕ is characterized by two apparent magnitudes v_1 and v_2 listed in Table 2: ϕ declines linearly from unity at magnitudes brighter than v_1 to zero fainter than v_2. ϕ vanishes for $b - y$ bluer than 0.21. For $b - y$ redder than 0.38, ϕ is reduced by a factor of 0.6.

The selection of Nordström et al. (2004) is designed to exclude red giant branch (RGB) stars from the data set. However, some of these stars are still in the sample, while the sample is biased against stars just below the giant branch. We take out of consideration the RGB itself, and downscale the theoretically expected population density near the starting point of the RGB by a factor of 4 to reconcile it with the data. Since the number of RGB stars in the GCS is not large anyway, the loss of information is small. We also removed from the data set three objects that are far too faint to be attributed to the main sequence. The theoretical distributions are convolved with a Gaussian of dispersion 0.1 dex in $[Z/\mathrm{H}]$ to allow for measurement errors.

Fig. 16 compares predicted (lower panel) and observed (upper panel) Hess diagrams for the GCS stars. As discussed by Holmberg et al. (2007), the ridge line of the main sequence in the GCS data is significantly displaced from that predicted by isochrones. We have eliminated the effects of this offset on Fig. 16 in the simplest possible way, namely by decreasing all model values of $\log(T_{\rm eff})$ by the value, 0.015, that yields the closest agreement between the theoretical and observation main sequences. After this correction has been made, the agreement between the theoretical and observational Hess diagrams shown in Fig. 16 is convincing though not perfect. The original conception had been to determine the model's

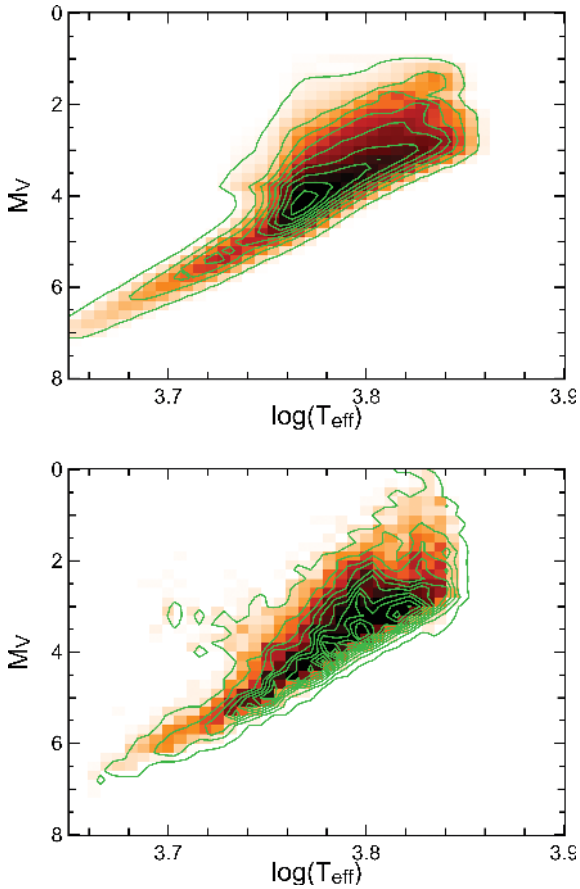

Figure 16. Comparison of the observed (upper) and predicted (lower) distributions of GCS stars in the ($T_{\rm eff}$, M_V) plane. Contours have an equal spacing of 10 counts per bin, starting with 3.

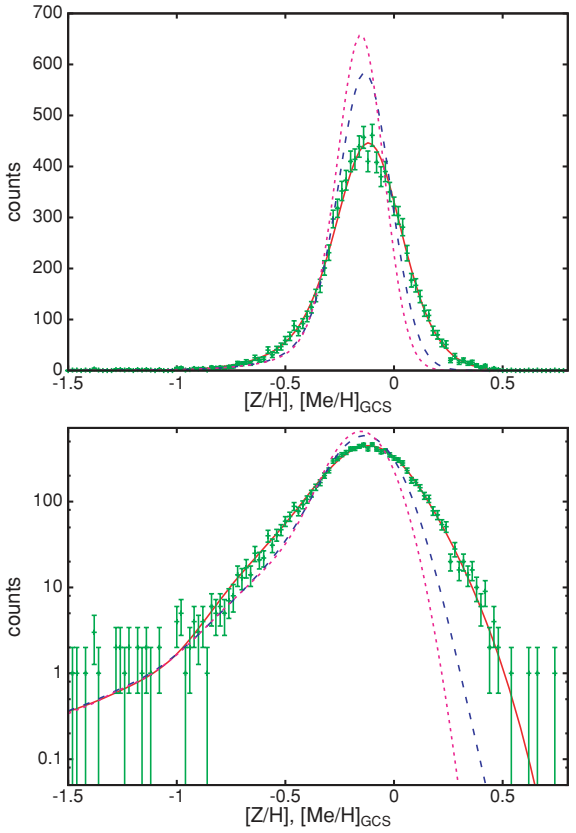

Figure 17. The metallicity distribution of GCS stars (green points) and the corresponding prediction of the standard model (full red curve). The broken blue curve shows the model that differs from the standard model only in the elimination of churning and radial gas flows. The broken pink curve shows the model with neither churning nor blurring. The lower panel shows the same data but with a logarithmic vertical scale to reveal structure in the wings of the distribution.

parameters by maximizing the likelihood of the GCS stars in the model density in (M_V, $T_{\rm eff}$, Z) space, but confidence in this plan was undermined by (i) the need for an arbitrary alignment of measured and theoretical values of $T_{\rm eff}$ and (ii) the extent to which the likelihood of the data depends on the uncertain GCS selection function. Notwithstanding these reservations, we are encouraged that the standard model maximizes the likelihood of the data at an age, $\sim$11 Gyr, that agrees with other estimates of the age of the solar neighbourhood (Aumer & Binney 2008, and references therein).

The full red curve in Fig. 17 shows the metallicity distribution of stars predicted by the standard model, and green points show the GCS data. The agreement is excellent. At the lowest metallicities, theory predicts slightly too few stars, but the uncertainties in both the theory and the data are large in this limit and the theory does not include halo stars, so it should underpredict the data at $[Z/{\rm H}] \lesssim -1$.

5 GENERAL TRENDS

We now discuss aspects of how the observable properties of a model depend on its parameters, and what is required to achieve fits of the quality seen in Figs 5 and 17.

Table 1 lists the model's 16 parameters; the third column explains whether the parameter is fitted to the GCS data or taken from the literature, and indicates the sensitivity of models to that parameter. Five parameters (M_0, M_1, b_1, $f_{\rm direct}$, $M_{\rm warm}$) significantly affect only the distribution of stars at $[Z/{\rm H}] < -0.7$. Six other parameters (M_2, t_0, k^{-1}, $t_{\rm cool}$, $Z_{\rm IGM}$) are fixed by observed properties of the Galaxy other than the solar-neighbourhood stellar distribution. The remaining five parameters are the critical surface density for star formation $\Sigma_{\rm crit}$, the long infall time-scale b_2, the accretion parameters $f_{\rm A}$ and $f_{\rm B}$, and the churning strength $k_{\rm ch}$. We shall see that $f_{\rm B}$ is effectively set by the metallicity gradient in the gas, that b_2 is effectively determined by the local Hess diagram and that the value of $\Sigma_{\rm crit}$ is unimportant provided it is small (we have included this parameter only for consistency with earlier work; the models do not want it). Consequently, the fit of the model to the data shown by the red curve and the green points in 17 is obtained by adjusting just $f_{\rm A}$ and $k_{\rm ch}$.

The number of stars more metal poor than $[Z/{\rm H}] \sim -1$ depends sensitively on the thermal structure of the early ISM. Most previous studies (exceptions include Thomas et al. 1998; Samland & Gerhard 2003) have used only one phase of the ISM. Introducing the warm component of the ISM delays the transfer of metals to the star-forming cold ISM by $\sim$1 Gyr, thus increasing the number of extremely metal-poor G dwarfs. Our first models initially had no warm gas, with the result that at early times the mass of warm gas was proportional to time and the metallicity of the cold gas rose quadratically with time. These models had an overabundance of *very* metal-poor stars. These experiments led to the conclusion that pregalactic and halo stars endowed the disc with warm, metal-rich gas at the outset. Even at late times, the existence of the warm ISM

delays the introduction of freshly made metals into stars, and thus in concert with the gas flow through the disc steepens the metallicity gradient in the stellar disc; eliminating the warm component raises the metallicity of the solar neighbourhood and beyond by ∼0.1 dex.

The metallicity of infalling gas only affects the structure of the disc at $R \gtrsim 12$ kpc. Lowering $Z_{\rm IGM}$ steepens the metallicity gradient at $R > R_0$.

It is instructive to consider the case in which blurring is included but churning is turned off by setting $k_{\rm ch} = 0$, and radial flows are eliminated by ensuring that $f_{\rm A} + f_{\rm B} = 1$ so every ring's need is fully supplied from the IGM. The broken blue curve in Fig. 17 shows the present-day metallicity distribution that this model predicts for the GCS. The peak of the distribution is much narrower than in the standard model, and there is a striking deficiency of metal-rich stars. The broken pink curve shows the effect of also turning off blurring: the deficiency of metal-rich stars becomes even more striking but there is negligible change on the metal-poor side of the peak.

Reducing the current SFR by making the infall rate a more rapidly declining function of time shifts the peak of the distribution to higher metallicities by reducing the relative strength of recent inflow and thus the supply of fresh, metal-poor gas. The use of an IMF that is steeper in the low-mass region, as has been suggested by some studies, reduces the mass of metals that is locked up in low-mass stars and increases the metal production by each generation. The metallicity in such a regime is accordingly higher, but the shape of the distribution does not change. Since changes in the IMF at the high-mass end, which is equally uncertain, can produce compensating variations in yields, loss rates, etc., we stayed with the traditional approach via the Salpeter IMF.

In all interesting models the metallicity of the local ISM saturates early on. The saturation level depends on the pattern of gas flow through the disc, and on the current SFR relative to the mean rate in the past: the faster the decline in the SFR, the higher the current metallicity. Naturally, the stars of the solar neighbourhood are on the average younger in models with a constant gas mass than in models in which the infall rate is declining according to equation (6). This relative youth is reflected in the structure of the local Hess diagram. We reject the model with constant gas mass because it assigns a significantly smaller likelihood to the Hess diagram of the GCS stars than does a model based on equation (6).

5.1 Selecting the standard model

All our models have quite strong metallicity gradients in both stars and gas (Figs 5 and 11). Since the metallicity of the central gas is enhanced by radial gas flow, and models with large $f_{\rm B}$ have larger central flows than models with large $f_{\rm A}$ and vice versa at large radii (Fig. 2), enhancing $f_{\rm B}$ steepens the metallicity gradient at small R and diminishes it at large R.

Eliminating churning and radial gas flows (by setting $k_{\rm ch} = 0$, $f_{\rm A} + f_{\rm B} = 1$) dramatically reduces the metallicity gradient within both the stellar and gas discs: at the present epoch the gradient in the gas near the Sun falls from -0.11 to -0.01 dex kpc^{-1}. Increasing the churning amplitude $k_{\rm ch}$ both increases the width of the peak in the predicted solar-neighbourhood metallicity distribution (Figs 11 and 17) and reduces the gradient in the mean metallicity of stars at $R \lesssim R_0$.

Fig. 18 shows how the likelihood of the GCS metallicity distribution plotted in Fig. 17 varies with $f_{\rm A}$, $f_{\rm B}$ and $k_{\rm ch}$. In the upper panel, favoured models (with large symbols) lie along a line that slopes down and to the right. Along this line, a decrease by 0.01 in $f_{\rm B}$ is compensated by an increase in $f_{\rm A}$ by ∼0.08.

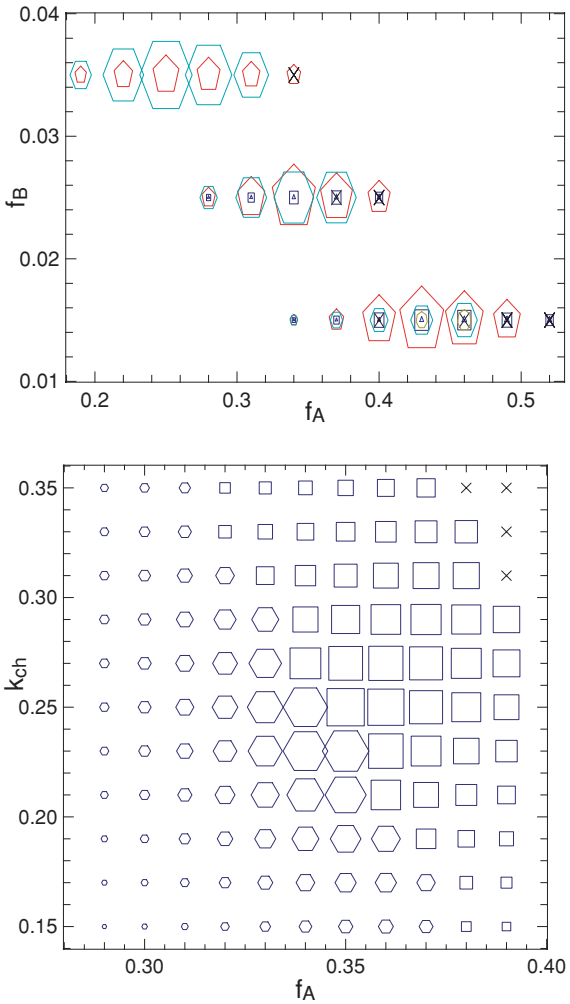

Figure 18. The likelihood of the GCS metallicity distribution in models with infall rates given by equation (6). Upper panel: the values of the infall parameters $f_{\rm A}$ and $f_{\rm B}$ are given by the locations of the symbols, and the value of $k_{\rm ch}$ is indicated by the number of sides of the polygon: 3, 4, 5, ... for $k_{\rm ch} = 0.0, 0.1, 0.2, \ldots$. The size of the polygon increases linearly with the log likelihood of the data; models with ages smaller than 9 Gyr are marked with crosses. Lower panel: the likelihoods of models with $f_{\rm B} = 0.025$ and varying ($f_{\rm A}$, $k_{\rm ch}$). In this panel, the size of a symbol is a more sensitive function of likelihood than in the upper panel. Hexagons indicate models with best-fitting ages higher than 12.6 Gyr; models with best-fitting ages below 9.6 Gyr are crossed.

As one moves down the upper panel of Fig. 18, the steepness of the metallicity gradient near the Sun increases, and the models with $f_{\rm B} = 0.015$ have local gradients steeper than -0.12 dex kpc^{-1}, which may conflict with the data. Models higher up the panel have smaller local metallicity gradients and require larger values of $k_{\rm ch}$ to bring a sufficient variety of stars to the solar neighbourhood. Models to the right of the panel have smaller inward flows of gas, leading to local metallicities that rise faster in time and they match the GCS metallicity distribution at younger ages, especially if $k_{\rm ch}$ is large so metal-rich stars migrate to the Sun relatively rapidly. The structure of the local Hess diagram for either GCS stars (Fig. 16) or *Hipparcos* stars (Aumer & Binney 2008) implies that the solar neighbourhood is not younger than 9 Gyr, so when the age is smaller than 9 Gyr the model is marked by a cross in Fig. 18. Models adjacent to

the crosses do not violate the 9 Gyr limit but are none the less disfavoured because their local Hess diagrams yield relatively low likelihoods for the GCS sample.

Four factors make it difficult to confine narrowly the required value of $k_{\rm ch}$ within the part of Fig. 18 that has large symbols: (i) churning affects mainly the width of the metallicity distribution, which has less impact on the likelihood than the location of its peak; (ii) churning, which is strongest in the inner regions of the disc, tends to saturate near the centre in the sense that old stars become fully shuffled; (iii) the GCS sample is biased against old and highly dispersed populations of stars, so where churning has the strongest effect, the observational signature is weak; (iv) the required churning strength is sensitive to the local metallicity gradient which is not very well constrained by observations.

In our models, there is no azimuthal variation in the metallicity of gas at a given radius, as is suggested by recent observations (see Nieva & Przybilla 2008), which yield very small to negligible inhomogeneity of the ISM at a given radius. The effect of relaxing this assumption can be gauged by increasing the dispersion in the measured metallicities of a given population of stars: if there is intrinsic dispersion in the metallicity of the ISM in a given annulus, the measured metallicities of stars formed from it will reflect both this dispersion and measurement errors. The largest intrinsic dispersion in the metallicity of the ISM that would appear to be compatible with the data plotted in Fig. 5 is ∼0.1 dex. When we combine this with measurement errors of 0.1 dex, we can obtain a fit to the GCS data of Fig. 17 that is only slightly worse than that provided by the standard model by lowering $k_{\rm ch}$ from 0.25 to ∼0.1.

We have studied models with several values of the mass-loss parameter $f_{\rm eject}$ and concluded that up to the largest values studied ($f_{\rm eject} = 0.15$ at $R < 3.5$ kpc and 0.05 elsewhere) $f_{\rm eject}$ does not have a large effect on the model's observable properties, and is anyway degenerate with the still uncertain nucleosynthetic yields. However, increasing $f_{\rm eject}$ makes it slightly easier to find an acceptable model, reflecting the fact that the yields we are using lie at the upper limit of the yields that are consistent with measured metallicities.

The upper panel of Fig. 19 shows the effect on the fit to the GCS metallicity distribution of using a non-zero value of the threshold gas density, $\Sigma_{\rm crit}$, below which the SFR declines steeply. Raising $\Sigma_{\rm crit}$ from zero to 2.5 $M_\odot$ pc^{-2} changes the model prediction from the red curve of the standard model to the blue curve; the distribution is now wider and peaks at lower metallicities. The pink dotted curve shows the result of maximizing the likelihood of the data subject to the constraint $\Sigma_{\rm crit} = 2.5\,M_\odot$ pc^{-2}. In this model, $f_{\rm A}$ is increased (to 0.44) and $k_{\rm ch}$ is decreased (to 0.20) relative to the standard model. The new model provides a slightly worse fit to the GCS data than the standard model, but, as the lower panel reveals, there is a problem with using a non-zero value of $\Sigma_{\rm crit}$: with minimal star formation in the outer disc, the metallicity gradient of the ISM steepens near the edge of the star-forming regions, while further out the metallicity becomes constant at the intergalactic value. The data show no sign of this plateau, and are probably incompatible with a plateau as low as $[Z/H] = -1$. Values of $\Sigma_{\rm crit} > 2.5\,M_\odot$ pc^{-2} are incompatible with the data because they bring the edge of the star-forming disc too close to the Sun.

By considering the likelihoods of both the Hess diagram and the metallicity distribution of GCS stars, and our prejudices regarding the proper value of $f_{\rm eject}$, we chose the model specified by Table 1 as the standard model. With this model, the likelihood of the GCS metallicity peaks at age 11.7 Gyr.

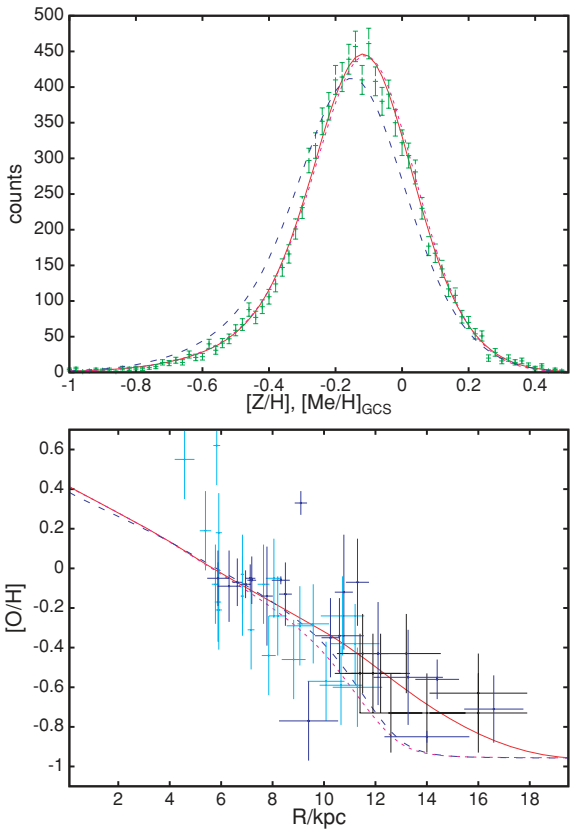

Figure 19. Upper panel: the data points are the GCS counts and the red curve is the standard model. The broken blue curve shows the effect on this model of raising $\Sigma_{\rm crit}$ from 0 to 2.5 $M_\odot$ pc^{-2}. The pink dotted curve shows that a good fit to the data can be obtained for this value of $\Sigma_{\rm crit}$. Lower panel: measurements of the metallicity of the ISM and the predictions of the models shown above.

6 RELATION TO OTHER WORK

Chemical evolution models of the Galaxy have a long history and a large literature. It would be inappropriate to attempt to review this literature in this section. Instead, we highlight crucial differences with work that has most in common with ours, and relate our work to the analysis of the solar neighbourhood of Haywood (2008).

6.1 Comparison with earlier models

Some of the best known models of Galactic chemical evolution are those in Chiappinin et al. (1997) and its successors (Chiappini et al. 2001; Colavitti et al. 2008). In each case, the disc is made up of annuli that exchange neither stars nor gas. Star formation is driven by a Kennicutt law similar to equation (1). Chiappinin et al. (1997) introduced a time-dependent infall rate that is superficially similar to (6) but differs from our infall rate in two important respects. First, the exponential with the longer time-constant is not turned on until 2 Gyr after the start of Galaxy formation with the consequence that star formation periodically ceases during the interval 1 Gyr $< t <$ 2 Gyr. Secondly, Chiappinin et al. (1997) make the time constant b_2 a linearly increasing function of radius that vanishes at $R = 0.86$ kpc (or 1.2 kpc in Chiappini et al. 2001), whereas here b_2 is constant. If we were to follow the prescription of Chiappini et al., our inner disc/bulge would become older, and a smaller churning rate would be required to bring stars more metal-rich than the local ISM to

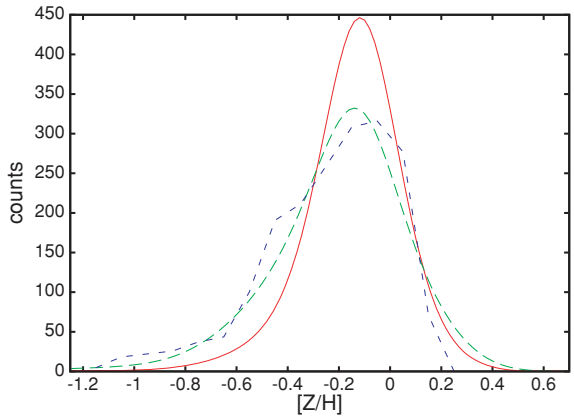

Figure 20. Full red curve: the metallicity distribution predicted by the standard model for the GCS stars. Long-dashed green curve: the prediction of the same model for the distribution of the whole solar annulus. Short-dashed blue curve: the prediction of Chiappinin et al. (1997) for the solar annulus.

the solar neighbourhood. An outwards-increasing infall time-scale enhances the metallicity gradient because metallicities are close to their equilibrium values, and these reflect the ratio of current to past SFRs.

Chiappinin et al. (1997) adjusted their model's free parameters to optimize its fit to the G-dwarf metallicity distribution for stars in the solar annulus that was determined by Rocha-Pinto & Maciel (1996) from 287 stars that lie within 25 pc of the Sun. Fig. 20 illustrates the difference between the metallicity distributions of stars near the Sun and in the entire solar annulus: the full red curve shows the standard model's prediction for the metallicity distribution of GCS stars from Fig. 17, while the long-dashed green curve shows the corresponding distribution in the whole annulus. The distribution for the annulus is much broader than that for the GCS because stars with metallicities far from that of the local ISM are typically fast-moving and likely to be at high z. Rocha-Pinto & Maciel (1996) transformed their measured distribution for the local sphere to the modelled global distribution using correction factors estimated by Sommer-Larsen (1991), which depend on the local gravitational potential and the velocity distributions of stars of each metallicity. It is clearly more satisfactory to use internally generated values of these distributions to predict the metallicity distribution in the observed volume around the Sun than to infer the annular distribution from the measured one using external estimates of the velocity distributions. Moreover, the short-dashed blue curve in Fig. 20 shows the prediction of Chiappinin et al. (1997) for the solar annulus. It declines much more steeply at high metallicities than the blue curve, predicting far too few metal-rich stars.

The scale of the discrepancy between the blue and the green curves illustrates that a model that provides an adequate fit to the data of Rocha-Pinto & Maciel (1996) is likely to be incompatible with the GCS stars. This discrepancy is partly due to problems with the calibration of the underlying data set: Haywood (2002) and Twarog, Anthony-Twarog & Tanner (2002) pointed out that the metallicity calibrations of Schuster & Nissen (1989) underlying those data sets severely underestimate the metallicities of metal-rich stars. This underestimation makes the decline in the number of stars at $[\,\mathrm{Fe/H}\,] > 0$ steeper than it should be, and thus makes it easier for the data to be fitted by traditional models of chemical evolution, which predict a sharp cut-off at high [Fe/H]. Apart from its superior calibration, the GCS sample is 50 times larger than that used by Rocha-Pinto & Maciel (1996), so its statistical errors are much smaller and it is a more challenging distribution to fit.

In the models of Chiappinin et al. (1997), star formation ceases entirely when the surface density of gas falls below $\Sigma_{\rm crit}$, while in our models $\Sigma_{\rm crit}$ merely marks an increase in the rate of decline of the SFR with decreasing gas density. While a cogent argument can be made for a rapid decline in the SFR at low gas densities, it is hard to justify a discontinuity in the rate. Chiappini et al. (2001) conclude that a non-negligible value of $\Sigma_{\rm crit}$ plays an essential role in fitting the data. In fact, they set $\Sigma_{\rm crit} = 7\,\mathrm{M}_\odot\,\mathrm{pc}^{-2}$, with the consequence that star formation in the solar neighbourhood was constantly stopping and starting, during both the first 2 Gyr and the last 4 Gyr of Galactic history (see their fig. 4). Since the metallicity of the ISM declines when star formation has been switched off, this erratic behaviour broadens the stellar metallicity distribution. In our models, the SFR is steady and in fact setting $\Sigma_{\rm crit} = 7\,\mathrm{M}_\odot\,\mathrm{pc}^{-2}$ would result in almost no stars forming at $R \gtrsim 10\,\mathrm{kpc}$ because the flow of gas through the disc would prevent the surface density building up to $7\,\mathrm{M}_\odot\,\mathrm{pc}^{-2}$. Hence, in our models star formation can occur at large radii only if $\Sigma_{\rm crit}$ is set to a small or vanishing value. An important difference between our models and those of Chiappini et al. (2001) is that in our models the SFR is a smooth function of time and the bimodality in $[\alpha/\mathrm{Fe}\,]$ is achieved without a dip in the SFR.

Chiappinin et al. (1997) give for the inner and outer parts of their models the radial gradients in the abundances of several elements. These gradients are largest in the inner regions, but even there they are much smaller than in our models: for example, at 12 Gyr the inner gradients of [O/H] and [Fe/H] are -0.023 and $-0.027\,\mathrm{dex\,kpc}^{-1}$ compared to values $\sim -0.08\,\mathrm{dex\,kpc}^{-1}$ and $\sim -0.11\,\mathrm{dex\,kpc}^{-1}$ obtained here. Our larger gradients are a direct consequence of the advection inwards of the products of nucleosynthesis. The GCS stars show a similar gradient in $[Z/\mathrm{H}]$: Holmberg et al. (2007) derive a gradient of $-0.09\,\mathrm{dex\,kpc}^{-1}$.

Colavitti et al. (2008) used infall rates measured from simulations of clustering cold dark matter (CDM) in slightly updated models of Chiappinin et al. (1997). No empirically determined infall rate gave such satisfactory results as the earlier double-exponential rate. The models were again compared to the metallicity distribution of Rocha-Pinto & Maciel (1996) and in most cases provided inadequate fits to the data. The empirically measured infall rates are very irregular in time, with the result that the model experiences powerful bursts of star formation. These lead to large excursions in the predicted plots of [O/Fe] versus [Fe/H] for which there is no evidence in the data. Moreover, studies of the past SFR in the disc show no signs of major bursts of star formation a few gigayears ago. The disappointing results of this study suggest that the rate at which gas joins the disc is not simply the ratio of masses of baryons and dark-matter times the dark-matter accretion rate. In fact, the wealth of evidence that the majority of baryons are still in the IGM (Persic & Salucci 1992; Fukugita, Peebles & Hogan 1998) is a clear indication that galaxies do not acquire gas as fast as this naive calculation suggests; rather gas is stored in the warm-hot intergalactic medium (WHIM) and from there accreted at a still uncertain rate. It seems unlikely that chemical evolution models will be successfully coupled to cosmological clustering simulations until we have understood the complex interface between the WHIM, cold infall and galactic fountains.

Naab & Ostriker (2006) determined the infall rate by assuming that the surface density of the disc is always exponential, but with a scalelength that is proportional to $v_{\rm c}/H$, where $v_{\rm c}$ is the Galaxy's circular speed (taken to be constant) and $H(t)$ is the Hubble

parameter. The infall rate at all times and places was fixed by assuming that the central surface density of the disc is constant at its current value. The model's observables were calculated by using the Kennicutt law (1) to convert gas to stars. A very simple approach to chemical evolution was employed, in which material does not move between annuli and only the overall metal content Z was followed. In these models, the metallicity gradient in the ISM becomes less steep over time, and is now $\sim -0.04\,\mathrm{dex\,kpc^{-1}}$. Their model predicts for the solar neighbourhood fewer metal-rich stars and more metal-poor stars than are in the GCS.

In all these models, solar-neighbourhood stars should satisfy a well-defined metallicity–age relation, and the G-dwarf metallicity distribution is simply the result of combining this relation with the SFR–age relation. As we have seen, the observed width of the local metallicity distribution is approximated by exploiting irregular time evolution of the metallicity of the local ISM (cf. also Portinari et al. 1998). As illustrated in Fig. 9, our models solve this problem in an entirely different way, and using a simpler history of star formation.

6.2 Haywood's analysis of the solar neighbourhood

Haywood (2006), and especially Haywood (2008), has critically re-examined the age–metallicity distribution of the GCS stars and concluded that the data are only consistent with the existence of a well-defined age–metallicity relation for disc stars younger than $\sim$3 Gyr; for such young stars the spread in [Fe/H] is consistent with the expected dispersion in the metallicity of interstellar gas at a given radius. At ages larger than 3 Gyr, the width of the metallicity distribution is larger than can be accounted for by measurement errors and inhomogeneity of the ISM. In particular, there are stars with ages $\sim$5 Gyr that have [Fe/H] $= 0.5$, and stars with ages $<$7 Gyr that have [Fe/H] $= -0.5$. The older the age bracket that one examines, the wider the range of metallicities present. Our predicted age–metallicity distribution (Fig. 6) is in good agreement with that derived by Haywood (2008).

Haywood (2006) finds that when his revised ages are used for GCS stars, the metallicities of thick-disc stars increase as their ages decrease. That is, these stars point to rapid self-enrichment of the thick disc. In fact, Haywood argues that the thick disc is not the relic of some captured satellite(s) but an integral part of the Galaxy's disc and has played a central role in the chemical evolution of the thin disc. Chemical evolution models should treat the disc as a whole, not just individual parts. Our results strongly underline this conclusion from a theoretical perspective. The metallicity–age plot shown in fig. 1(b) of Haywood (2008) is satisfyingly similar to the lower panel of our Fig. 6: in both figures, the stellar density is highest around ($\tau = 2$ Gyr, [Fe/H] $= -0.1$), and in this region the ridge line gradually drops to the right. At older ages, the distributions become broader, being confined by [Fe/H] ~ 0.4 and -0.5. At ages greater than 10 Gyr, both distributions reach down to [Fe/H] $= -1$. In fact, the small differences between our figure and that of Haywood are readily accounted for by the substantial errors in measured stellar ages. This fit is remarkable because the model parameters were chosen without reference to measured stellar ages.

An argument sometimes advanced for a dichotomy between the thick and thin discs is the existence of two sequences in the ([α/Fe], [Fe/H]) plane (Fig. 9). This diagram suggests that the last thick-disc stars to form had higher abundances than the first thin-disc stars to form. To explain this finding in the context of a conventional chemical evolution model, sudden dilution of the ISM by a massive gas-rich accretion is required (Bensby et al. 2005; Reddy, Lambert & Allende Prieto 2006). Against this proposal, Haywood (2006) objects that the bulk of the oldest thin-disc stars have [Fe/H] $\simeq -0.2$ and there is no evidence that the most metal-poor thin-disc stars are particularly old. Our models show that the observed structure of the ([α/Fe], [Fe/H]) plane arises naturally when radial migration is allowed. Haywood (2008) examined the orbital parameters of stars of various metallicities and showed that local thin-disc stars with metallicities that overlap the metallicity range of the thick disc have higher angular momenta than more typical thin-disc stars. Similarly, he found that stars in the high-metallicity tail of the local metallicity distribution have low angular momenta. Even though churning could in principle eradicate the correlation between angular momentum and metallicity, our models reproduce these correlations (Figs 9 and 10) because blurring makes a sufficiently large contribution to bringing these chemically anomalous stars near the Sun.

Ivezic et al. (2008) also argue that in the SDSS data the kinematic properties of the thick disc evolve continuously with distance from the plane in a way that suggests that the thick disc joins continuously to the thin disc. By contrast, Veltz et al. (2008) argued for a clean break between the thin and thick discs on the basis of shallow local minima in the density of 2MASS stars $n(z)$ seen at the Galactic poles as a function of photometric distance z. As Veltz et al. (2008) show, minima in $n(z)$ are not expected if the disc is a superposition of two exponential structures, but the minima yield a clean discontinuity in the distribution of velocity dispersions when multi-component isothermal DFs are used to model the data. The very unexpectedness of the minima makes the modelled break extremely clean. It will be interesting to see whether the distribution of measured radial velocities of stars in the Radial Velocity Experiment (RAVE) survey substantiates these model velocity distributions.

7 CONCLUSIONS

It is now more than 40 years since the theory of stellar evolution attained the level at which it became possible to model the chemical enrichment of the ISM. From the beginning of that endeavour, measurements of the abundances of individual solar-neighbourhood stars have played a key role because a star preserves like a time capsule the state of the ISM at the remote epoch of its formation. Considerable theoretical and observational efforts have been devoted to probing the history of the Galaxy with this connection.

Half a century ago, Roman (1950, 1954) and others discovered the connection between the kinematics and chemistry of stars, yet curiously little has been done to include kinematics in models of chemical evolution. The general presumption has been that each annulus of the disc evolves independently of others, and the well-known correlations between chemistry and kinematics can be understood as arising through the stochastic acceleration of stars: older stars tend to have larger random velocities and lower metallicities. No effort was made to develop greater diagnostic power by simultaneously modelling chemistry and kinematics.

The continued use of mutually independent annuli by modellers of chemical evolution is surprising given that it was from the outset recognized that many stars are on significantly non-circular orbits that each radial half-period cover more than a kiloparsec in radius. In fact, it has generally been assumed that the radial velocity dispersion within the disc rises as one moves inwards to values that lead to radial excursions of several kiloparsec (see Fig. 4). Moreover, observations have long indicated that galactic discs have significant metallicity gradients (e.g. Vila-Costas & Edmunds 1992; de Jong 1996), so radial migration of stars is bound to leave a signature on

the metallicity distribution of solar-neighbourhood stars. We have called this aspect of radial migration 'blurring'.

The present study owes its impetus to the discovery by Sellwood & Binney (2002) that radial migration is a more potent process than mere blurring: the dominant effect of transient spiral arms is not to heat the stellar disc as had been supposed, but to cause stars either side of corotation to change places without moving to eccentric orbits ('churning'). Sellwood & Binney (2002) did not demonstrate that gas participates in churning, but they argued that it must on dynamical grounds, and Roskar et al. (2008a) found evidence that this was the case in their N-body–SPH simulations of galaxy formation. Since churning is an aspect of spiral structure that can *only* be probed through its impact on chemical evolution, we wanted chemical evolution models that included churning, and logically it was natural to extend these models to include both blurring and radial gas flows.

An ingredient of our models that might be controversial is the introduction of radial gas flows. We have absolutely no reason to expect that the infall profile is exponential, so if discs are to be exponential this must be the result of flows through the discs redistributing mass within the disc. In fact, as gas streams through spiral arms it dissipates energy in shocks that is ultimately gravitational energy that becomes free as the gas surrenders angular momentum to the stars and drifts inwards. Hence, at some level inward gas flows are mandatory (Lacey & Fall 1985).

Unfortunately, the theory of galaxy formation has yet to advance to the point at which it can prescribe the spatial and temporal structure of gas accretion, so it is necessary to parametrize accretion in some way. The accretion process must be constrained to result in the formation of the observed stellar and gaseous discs. Our accretion Scheme AB satisfies this constraint for all values of the parameters, but it is inevitably acausal in that the formation mechanism is being driven by its known outcome. While its acausality is unattractive, Scheme AB is a flexible parametrization that enables us to form exponential discs for a variety of different assumptions about the radial density of infalling gas, and the resulting radial profiles of infall and gas flow (Fig. 2) are entirely plausible.

The impact that radial migration has on the local metallicity distribution obviously varies with the magnitude of the metallicity gradient in the ISM, which in turn depends on the gas flow within the disc and therefore the radial infall profile. For this reason, the most important parameters of our models are $f_{\rm A}$ and $f_{\rm B}$, which control the distribution of infalling gas.

The models provide good fits to the GCS counts of stars as functions of [Fe/H], M_V, $T_{\rm eff}$ and stellar age, as well as reproducing the correlations between tangential velocity and abundance patterns that have been pointed out by Haywood (2008). These fits are achieved by churning, blurring and radial flows working together. They depend on the existence of an appreciable metallicity gradient in the ISM, which is established by the radial flow of gas, and they depend on radial mixing of stars by blurring and churning. The steeper the metallicity gradient in the gas, the smaller the effect of churning can be, but for any observationally consistent metallicity gradient, churning has a non-negligible role to play.

The models describe the coevolution of the thick and thin discs, and presume that thick-disc stars were formed in the Galaxy rather than accreted from outside. Given the simplicity of our assumptions, the extent to which a dichotomy between an α-enhanced thick disc and a solar-type thin disc automatically manifests itself in the models is remarkable. In particular, in the solar annulus the distributions of [O/H] at given [Fe/H] are bimodal in the range of [Fe/H] associated with the overlap of the two discs (Fig. 9), the vertical density profile can be represented at the sum of two exponentials and at $R < R_0$ the radial density profile becomes flatter at lager distances from the plane (Fig. 8). None of these characteristics is dependent on our choice of a double exponential for the time dependence of infall: a model in which the gaseous mass, and therefore SFR, is held constant also has these features. They are consequences of the ~ 1 Gyr time-scale of Type Ia supernovae and the secular heating and churning of the disc.

The models assume that scattering of stars increases the velocity dispersion of a coeval population as $t^{1/3}$, but the models go on to predict that within the solar neighbourhood velocity dispersion increases as a higher power of age, roughly $t^{0.45}$ in agreement with what is found from *Hipparcos* stars with good parallaxes. This finding may reconcile scattering theory, which cannot readily explain an exponent in excess of 1/3, with observations. The key point is that radial mixing brings to the solar-neighbourhood stars born at small radii, where the velocity dispersion is undoubtedly large.

The nucleosynthetic yields from each generation of stars are still significantly uncertain. Our philosophy has been to use standard values from the literature rather than exploit uncertainties in the yields to tune the models to the data. The yields we are using are in the upper region of those that can provide adequate fits to the data, with the consequence that increasing the value of the mass-loss parameter $f_{\rm eject}$, which is degenerate with the magnitude of the yields, makes it easier to fit the data. Our yields are surely not exactly right and consequently some of the properties the models derive from them will be in error. On account of these uncertainties, we have suppressed the predictions of our code for the abundances of certain elements, most notably carbon.

The discovery that three-dimensional, non-equilibrium models of the solar atmosphere require the metal abundance of the Sun to be $Z_\odot = 0.012$–0.014 (Grevesse et al. 2007) poses a major problem for this field. A prerequisite for successful chemical modelling is a consistent metallicity scale for both stars and the ISM. At present, the only consistent scale is the traditional one on which $Z_\odot = 0.019$, so this is the one we have used.

If a new scale were established on which all metallicities were significantly lower, viable models could be produced by lowering the yields. A straightforward way to do this would be to lower the maximum mass in the IMF: reducing this mass from $100\,{\rm M}_\odot$ to $50\,{\rm M}_\odot$ would reduce yields by $\sim$30 per cent in line with the proposed reduction in $Z_\odot$. The oxygen yield would come down fastest, reducing [O/Fe] by ~ 0.2 dex.

Although we believe that this study represents a significant advance on all previous models of Galactic chemical evolution, it is highly imperfect. Some major weaknesses of our work are the following.

(i). We have assumed that the probability of mass interchange between rings is proportional to the product of the rings' masses. This probability reflects the number and intensity of spiral feature with corotation at that radius, and should be a function of both mass and velocity dispersion. A further study of self-gravitating discs similar to that of Sellwood & Binney (2002) would be necessary to determine this function.

(ii). We have assumed that the vertical and radial motions of stars decouple. This assumption has a significant impact on both the relation between age and velocity dispersion in the solar neighbourhood and on the predicted vertical density profile in the solar annulus, which is interesting in itself and impacts on the selection function of GCS stars and thus on our choice of standard model. The assumption is unjustifiable for stars on eccentric orbits, which

do play an important role in the model fits. Unfortunately, a sounder treatment is impossible until a better approximation to the third integral of Galactic dynamics is available. It is our intention to resolve this problem through 'torus modelling' (e.g. McMillan & Binney 2008).

(iii). Our models include radial mixing of gas through churning and viscous inspiralling, but do not include radial redistribution of gas by the Galactic fountain (e.g. Benjamin & Danly 1997). A significant body of evidence indicates that star formation drives neutral hydrogen to kiloparsec heights above the plane. NGC 891, which is not dissimilar to the Galaxy, has ∼25 per cent of its neutral hydrogen more than 1 kpc from the plane (Oosterloo et al. 2007). This extraplanar gas must move over the plane on nearly ballistic trajectories, and in the absence of interaction with the corona (gas at the Galaxy's virial temperature $\sim 2 \times 10^6$ K), the gas must return to the plane further out than its point of ejection. However, observations suggest that neutral gas above the plane is actually flowing inwards rather than outwards, presumable as a result of interaction with the corona (Fraternali & Binney 2008). The mass of extraplanar gas is so large and the time-scale for its return to the plane so short that whichever way this gas flows, it has a considerable potential for radially redistributing metals. Extraplanar gas must be ejected from the disc by supernova-heated gas that is probably highly metal-rich. Some of this gas will be lost to the Galaxy as we have assumed, but some of it will return to the plane with infalling gas. Again, there is potential here for significant radial redistribution of metals that has been ignored in the present study.

(iv). Our treatment of the inner Galaxy is unacceptably crude in that we have replaced the bar/bulge with a disc. Unfortunately, introducing the bar opens a Pandora's box of complexities, and at the present time is probably only feasible in the context of a particle-based model such as those of Samland & Gerhard (2003) and Roskar et al. (2008b). Our hope is that our imaginary central disc has a similar impact on the chemodynamical state of the local disc to the combined impact of the giant star-forming ring at $R \simeq 4$ kpc, the gas-deficient region interior to this ring and the star-forming x_2 disc at $R \lesssim 200$ pc.

From this list of shortcomings of our models, it is clear that we are still far from a definitive account of the Galaxy's chemical evolution. We shall be satisfied if we have convinced the reader that the interplay between dynamics and chemistry is so tight that it is indissoluble. This fact is at one level inconvenient because it undermines the value of conclusions drawn from traditional models of chemical evolution. But at another level, it represents an opportunity to learn more. The connection between the kinematics of stars and the compositions of stars and gas, which can be measured in great detail, involves three areas about which we are too ignorant: the distribution of dark matter within and around the Galaxy, the Galaxy's history of assembly and the nature of the Local Group's IGM. By building dynamical models of the Galaxy that have chemical evolution built in to the basic structure, we should be able to make decisive progress with one of the major problems of contemporary astronomy.

ACKNOWLEDGMENTS

We thank M. Haywood, J.-U. Ness and A. Riffeser for fruitful discussions. RS acknowledges material and financial support from the Studienstiftung des Deutschen Volkes and Stiftung Maximilianeum and the hospitality of Merton College Oxford, where this work began.

REFERENCES

Aumer M., Binney J., 2008, MNRAS, submitted
Benjamin R. A., Danly L., 1997, ApJ, 481, 764
Bensby T., Feltzing S., Lundström I., Ilyin I., 2005, A&A, 433, 185
Binney J., Lacey C., 1988, MNRAS, 230, 597
Binney J., Dehnen W., Bertelli G., 2000, MNRAS, 318, 658
Bland-Hawthorn J., Cohen M., 2003, ApJ, 582, 246
Chiappini C., Matteucci F., Gratton R., 1997, ApJ, 477, 765
Chiappin C., Matteucci F., Romano D., 2001, ApJ, 554, 1044
Chieffi A., Limongi M., 2004, ApJ, 608, 405
Colavitti E., Matteucci F., Murante G., 2008, A&A, 483, 401
Daflon S., Cunha K., 2004, ApJ, 617, 1115
Dehnen W., 1998, AJ, 115, 2384
Dehnen W., 1999, AJ, 118, 1201
Dehnen W., Binney J., 1998, MNRAS, 298, 387
de Jong R. S., 1996, A&A, 313, 377
Edvardsson B., Andersen J., Gustafsson B., Lambert DL., Nissen P. E., Tomkin J., 1993, A&A, 275 101
Flynn C., Holmberg J., Portinari L., Fuchs B., Jahreiss H., 2006, MNRAS, 372, 1149
Förster F., Wolf C., Podsiadlowski Ph., Han Z., 2006, MNRAS, 368, 1893
Francois P., Matteucci F., Cayrel R., Spite M., Spite F., Chiappini C., 2004, A&A, 421, 613
Fraternali F., Binney J., 2008, MNRAS, 386, 935
Fukugita M., Peebles P. J. E., Hogan C. J., 1998, ApJ, 503, 518
Grevesse N., Asplund M., Sauval A. J., 2007, SSRv, 130, 105
Haywood M., 2002, MNRAS, 337, 151
Haywood M., 2006, MNRAS, 371, 1760
Haywood M., 2008, MNRAS, 388, 1175
Holmberg J., Nordström B., Andersen J., 2007, A&A, 475, 519
Ivezic Z. et al., 2008, ApJ, 684, 287
Iwamoto K., Brachwitz F., Nomoto K., Kishimoto N., Umeda H., Hix W., Thielemann F.-K., 1999, ApJS, 125, 439
Juric M., Ivezić Z., Brooks A. et al., 2008, ApJ, 673, 864
Just A., Jahreiss H., 2007, preprint (arXiv0706.3850)
Kalberla P. M. W., Dedes L., 2008, A&A, 487, 951
Kennicutt R. C., 1998, ApJ, 498, 541
Kharchenko N. V., Piskunov A. E., Röser S., Schilbach E., Scholz R.-D., 2005, A&A, 438, 1163
Kregel M., van der Kruit P. C., 2005, MNRAS, 358, 481
Lacey C. G., Fall S. M., 1985, ApJ, 290, 154
Lai D. K., Bolte M., Johnson J. A., Lucatello S., Heger A., Woosley S. E., 2008, ApJ, 681, 1524
Limongi M., Chieffi A., 2008, http://orfeo.iasf-roma.inaf.it/
Linsky J. L. et al., 2006, ApJ, 647, 1106
Loktin A. V., Beshenov G. V., 2003, Astron. Rep., 47, 6
McMillan P., Binney J., 2008, MNRAS, 390, 429
Maeder A., 1992, A&A, 264, 105
Marigo P., 2001, A&A, 370, 194
Naab T., Ostriker J. P., 2006, MNRAS, 366, 899
Nordström B. et al., 2004, A&A, 418, 989
Oosterloo T., Fraternali F., Sancisi R., 2008, AJ, 134, 1019
Pagel B. E. J., 1997, Nucleosynthesis and Chemical Evolution of Galaxies. CUP, Cambridge
Persic M., Salucci P., 1992, MNRAS, 258, 14
Pettini M., Madau P., Bolte M., Prochaska J. X., Ellison S. L., Fan X., 2003, ApJ, 594, 695
Pietrinferni A., Cassisi S., Salaris M., Castelli F., Cordier D., Castellani M., 2004, ApJ, 612, 168
Pizagno J. et al., 2005, ApJ, 633, 844
Portinari L., Chiosi C., Bressan A., 1998, A&A, 334, 505
Nieva M. F., Przybilla N., 2008, A&A, 481, 199
Reddy B. E., Lambert D. L., Allende Prieto C., 2006, MNRAS, 367, 1329
Rich R. M., Howard C., Reitzel D. B., Zhao H.-S., de Propris R., 2007, in Bureau M., Althanassoula E., Barbuy B., eds, Proc. IAU Symp. 245, Formation and Evolution of Galaxy Bulges. Cambridge Univ. Press, Cambridge, p. 333

Robin A. C., Reylé C., Derrière S., Picaud S., 2003, A&A, 409, 523
Rocha-Pinto H. J., Maciel W. J., 1996, MNRAS, 279, 447
Rolleston W. R. J., Smartt S. J., Dufton P. L., Ryans R. S. I., 2000, A&A, 363, 537
Roman N. G., 1950, ApJ, 112, 554
Roman N. G., 1954, AJ, 59, 307
Roskar R., Debattista V. P., Stinson G. S., Quinn T. R., Kaufmann T., Wadsley J., 2008a, 675, L65
Roskar R., Debattista V. P., Quinn T. R., Stinson G. S., Wadsley J., 2008b, 684, L79
Samland M., Gerhard O. E., 2003, A&A, 399, 961
Sancisi R., Fraternali F., Oosterloo T., van der Hulst T., 2008, A&AR, 15, 189
Schmidt M., 1963, ApJ, 137, 758
Schuster W. J., Nissen P. E., 1989, A&A, 221, 65
Sellwood J. A., Binney J., 2002, MNRAS, 336, 785
Shaver P. A., McGee R. X., Newton L. M., Danlks A. C., Pottasch S. R., 1983, MNRAS, 204, 53
Shu F. H., 1969, ApJ, 158, 505
Sommer-Larsen J., 1991, MNRAS, 249, 368
Thomas D., Greggio L., Bender R., 1998, MNRAS, 296, 119
Twarog B. A., Anthony-Twarog B. J., Tanner D., 2002, AJ, 123, 2715
van den Bergh S., 1962, AJ, 67, 486
van der Kruit P. C., Searle L., 1982, A&A, 110, 79
van Woerden H., Wakker B. P., 2004, in van Woerden H., Wakker B. P., Schwarz U. J., de Boer K. S., eds, High Velocity Clouds. Kluwer, Dordrecht, p. 195
Veltz L., Bienaymé O., the RAVE Collaboration, 2008, A&A, 480, 753
Venn K. A., Irwin M., Shetrone M. D., Tout C. A., Hill V., Tolstoy E., 2004, AJ, 128, 1177
Vila-Costas M. B., Edmunds M. G., 1992, MNRAS, 259, 121
Vilchez J. M., Esteban C., 1996, MNRAS, 280, 720

APPENDIX: ORIGIN OF BIMODAL [O/Fe] DISTRIBUTIONS

We provide an analytic model of the development of the bimodal distributions of [O/Fe] evident in Fig. 9. We assume that star formation starts at $t = 0$ and that the SFR is $\propto \mathrm{e}^{-Kt}$ for $t > 0$. Consistent with equation (5), we assume that a coeval group of stars formed at t' generates a rate of Type Ia supernovae that vanishes for $t < t' + t_0$ and is subsequently $\propto \mathrm{e}^{-k(t-t')}$. Then, given that the rate of core-collapse SNe is proportional to the SFR, the rate of production of Fe is

$$\frac{\mathrm{d}M_{\rm Fe}}{\mathrm{d}t} = \begin{cases} b\mathrm{e}^{-Kt} & \text{for} \quad t < t_0 \\ b\mathrm{e}^{-Kt} + c\int_0^{t-t_0} \mathrm{d}t'\, \mathrm{e}^{-Kt'}\mathrm{e}^{-k(t-t')} & \text{for} \quad t \geq t_0, \end{cases} \tag{A1}$$

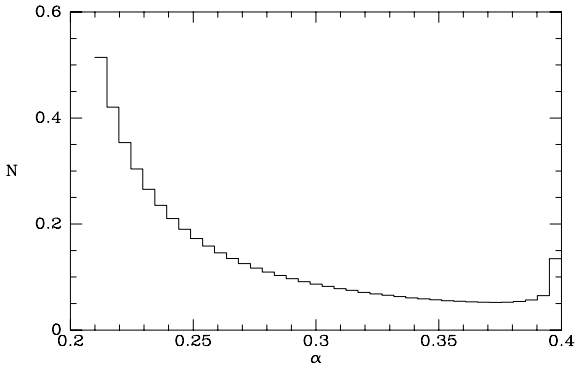

Figure A1. The distribution of α-abundances predicted by equation (A2).

where b and c are constants. Integrating this production rate, we obtain the iron mass at time $t > t_0$ as

$$M_{\rm Fe}(t) = b\frac{1-\mathrm{e}^{-Kt'}}{K} + \frac{c}{k-K}\left(\mathrm{e}^{-(k-K)t_0}\frac{\mathrm{e}^{-Kt_0}-\mathrm{e}^{-Kt}}{K} - \frac{\mathrm{e}^{-kt_0}-\mathrm{e}^{-kt}}{k}\right). \tag{A2}$$

In the approximation that SNIa do not contribute α-elements, and that the delay in the production of these elements by a stellar population is $\ll 1/k$, the mass of α-elements is $M_\alpha = (1-\mathrm{e}^{-Kt})a/K$ where a is a constant. Then, equation (A2) predicts that $\alpha \equiv M_\alpha/M_{\rm Fe}$ equals a/b for $t \leq t_0$ and then drops rapidly towards its asymptotic value,

$$\alpha(\infty) = \frac{b}{K} + \frac{c}{Kk}\mathrm{e}^{-kt_0}. \tag{A3}$$

Fig. A1 plots the distribution at $t = 13$ Gyr of stars over α when the initial and asymptotic values of α are set to 0.4 and 0.2 and the other parameters are $K = 1/7$ Gyr, $k = 1/1.5$ Gyr and $t_0 = 0.3$ Gyr, which allows 0.15 Gyr for white dwarfs to form and 0.15 Gyr for them to accrete prior to deflagrating.

This paper has been typeset from a TEX/LATEX file prepared by the author.